

Measurement of ${}^3_{\Lambda}\text{H}$ lifetime in Au+Au collisions at the Relativistic Heavy-Ion Collider

Analysis Note

PAs: Yifei Xu, Yuhui Zhu, Jinhui Chen, Zhangbu Xu, Yugang Ma, Declan Keane

Abstract

A precise measurement of the ${}^3_{\Lambda}\text{H}$ lifetime from a combined analysis of its two mesonic decay channels is presented: ${}^3_{\Lambda}\text{H} \rightarrow {}^3\text{He} + \pi^-$ and ${}^3_{\Lambda}\text{H} \rightarrow d + p + \pi^-$ based on Au+Au collision data collected in the years 2010 and 2011 by the STAR collaboration at RHIC. A minimum χ^2 estimation is used to determine the lifetime of ${}^3_{\Lambda}\text{H}$, yielding the result $\tau = 142^{+24}_{-21} \text{ (stat.)} \pm 31 \text{ (syst.) ps}$. The decay branching ratios have the property $\text{B.R.}({}^3\text{He} + \pi^-) / (\text{B.R.}({}^3\text{He} + \pi^-) + \text{B.R.}(d + p + \pi^-)) = 0.32 \pm 0.05 \text{ (stat.)} \pm 0.08 \text{ (syst.)}$. Our updated measurement indicates that ${}^3_{\Lambda}\text{H}$ has a significantly shorter lifetime than free Λ , namely $263 \pm 2 \text{ ps}$.

Contents

1	Introduction	4
1.1	Topological Map	5
2	Data Selection	6
2.1	Three Body Part	6
2.1.1	Event Level	6
2.1.2	Track Level Basic Cuts	6
2.1.3	Particle Identification	6
2.1.4	Signal Extraction	8
2.2	Two Body Part	8
2.2.1	Event-level cuts and statistics	19
2.2.2	^3He PID	19
2.2.3	π PID	20
2.2.4	Signal Extraction	20
3	$^3_\Lambda\text{H}$ signal	23
3.1	Three Body Part	23
3.1.1	Invariant Mass	23
3.1.2	Signal Counts	23
3.2	Two Body Part	24
3.2.1	Signal and background counting	24
3.2.2	Signals reconstructed in separate datasets	25
3.2.3	Combined Signal QA	25
3.2.4	Signal Counts	26
4	Embedding	30
4.1	Three Body Part	30
4.2	Two Body Part	31
4.2.1	Embedding QA	31
4.2.2	Embedding Rapidity Correction	32
4.2.3	Efficiency	33
5	Lifetime Analysis	34
6	Ratio Analysis	36
7	Systematic Uncertainty	37
7.1	Three Body Part	37
7.1.1	Binning Effect	37
7.1.2	DCA between proton and pion	38

7.1.3	DCA Between (virtual) Lambda and Primary Vertex .	38
7.1.4	Other sources	38
7.2	Two Body Part	39
7.2.1	Topological cuts and binning	39
7.2.2	Interaction with Material	40
7.2.3	interaction with air	40
7.2.4	Interaction with detector structure material	40
7.3	Summary	40
8	World Lifetime and Discussion	42

1 Introduction

The hyperon-nucleon (Y-N) interaction is of fundamental interest because it introduces the strangeness quantum number in nuclear matter [1]. Understanding the Y-N interaction can provide insights into the QCD theory of the flavor SU(3) group [2]. The Y-N interaction is also predicted to be of crucial importance in some high-density matter systems, such as neutron stars [3, 4]. It has become extremely difficult to describe neutron stars exceeding two solar masses, as observed recently [5, 6], because realistic relativistic equations that contain hyperons become soft at high densities. Among other explanations (such as deconfinement to quark matter), alternative Y-N couplings have been suggested as possible solutions for the so-called “hyperon puzzle” [7–9]. Due to the absence of stable hyperon beams, our current understanding of the Y-N interaction is very limited. Hypernuclei are natural hyperon-baryon correlation systems and can be used as an experimental probe to study the Y-N interaction. The lifetime of a hypernucleus depends on the strength of the Y-N interaction [10, 11]. Therefore, a precise determination of the lifetime of hypernuclei provides direct information on the Y-N interaction strength [11, 12].

The hypertriton ${}^3_{\Lambda}\text{H}$, which consists of a Λ , a proton and a neutron, is the lightest known hypernucleus. Some authors argue that the lifetime of the ${}^3_{\Lambda}\text{H}$ should be close to that of the free Λ -hyperon, since the ${}^3_{\Lambda}\text{H}$ is thought to be a Λ weakly bound to the deuteron core [13]. The lifetime of the ${}^3_{\Lambda}\text{H}$ has been measured using helium bubble chambers or nuclear emulsion, beginning in the 1960s [14–20]. The first measurement from a helium bubble chamber experiment yielded $\tau({}^3_{\Lambda}\text{H}) = 95^{+19}_{-15}$ ps [14]. Subsequent measurements indicated a lifetime close to [16, 17, 19, 20] or shorter than [15, 18] that of the free Λ , though with large statistical uncertainty. Recently, measurements of the ${}^3_{\Lambda}\text{H}$ lifetime using the Relativistic Heavy-Ion Collider (RHIC) at BNL, using HypHI at GSI, and using the Large Hadron Collider at CERN were reported [21–23], which all show a shorter lifetime than that of the free Λ . However, the dispersion of the different estimates do not allow a clear conclusion on the lifetime of the ${}^3_{\Lambda}\text{H}$ to be reached. Moreover, theoretical calculations do not provide a consensus picture because of diverging lifetime values [10, 11, 13, 24–29].

In this paper, we report new precise measurement of the ${}^3_{\Lambda}\text{H}$ lifetime from the Solenoid Tracker at RHIC (STAR) experiment. RHIC provides an ideal laboratory to study the Y-N interaction because hyperons and nucleons are abundantly produced in high-energy nucleus-nucleus collisions [21]. The main detector of STAR [30] is a time projection chamber (TPC) [31], which measures momentum and energy loss of outgoing particles. This information

is used to identify charged particles, like π^\pm , p , d and ${}^3\text{He}$ produced in the collisions. We are able to reconstruct ${}^3_\Lambda\text{H}$ via its two main decay channels: the ${}^3_\Lambda\text{H} \rightarrow {}^3\text{He} + \pi^-$ and the ${}^3_\Lambda\text{H} \rightarrow d + p + \pi^-$ at STAR. Due to very small decay branching ratios, or decays into neutral particles [11], the remaining channels have been disregarded in this analysis.

1.1 Topological Map

The ${}^3_\Lambda\text{H}$ has several decay channels. In this analysis, we focus on the three-body and two-body pionic decay modes. The figure 1 shows the decay topology.

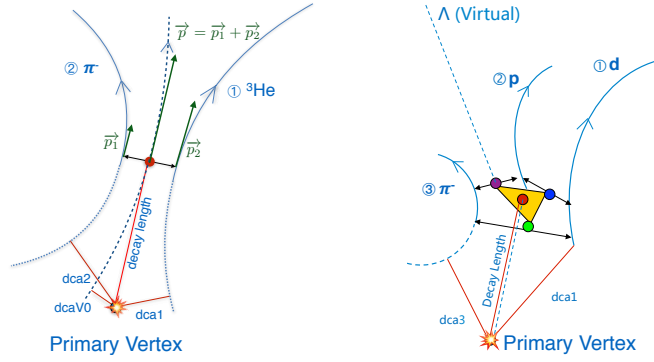


Figure 1: The left panel shows the decay topology of two body channel. The right panel shows the decay channel of the three-body channel.

We use following steps to determine the V0 position and topological cuts in three body analysis:

- (1) define the three daughter tracks as daughter 1(deuteron),daughter 2(proton) and daughter 3(pion).
- (2) find the DCA points between daughter 1-2, 1-3 and 2-3, then connect these points to form three segments.
- (3) use the mid-points of three segments to form a triangle.
- (4) define the center of gravity of this triangle as the decay point of hyper triton. This decay point is marked as v0123.
- (5) find DCA points between v0123 and one of daughters. The momentum of v0123 will be sum of daughter momenta at DCA points.
- (6) use position and momentum of v0123 to form a helix. Then defined the decay length and DCA of hyper triton.

2 Data Selection

2.1 Three Body Part

In this analysis, we used minimum bias data from Run11 27GeV, Run10 39GeV and Run11 200GeV for three body decay analysis.

2.1.1 Event Level

In table 1 we listed the event level cuts as well as centrality selection, trigger type, trigger ID and total statistics. We use class "RefMultCorr" to reject bad runs and to determine centrality.

Table 1: Database for the 3-body decay channel analysis.

Run	Energy	Vr(cm)	Vz(cm)	Centrality	Trigger Type	Event #
Run11	27 GeV	≤ 2.0	≤ 50	[1,16]	MB	53.31M
Run10	39 GeV	≤ 2.0	≤ 40	[1,16]	MB	134.41M
Run11	200 GeV	≤ 2.0	≤ 30	[1,16]	MB	516.87M

2.1.2 Track Level Basic Cuts

On track level, we use multiple cuts to select signal candidates. The detailed track level cuts are listed in the figure 2. Basically, the nHitFit, nHitsDedx, η , p_T , track flag and charge cuts are all commonly used cuts, so we won't spend much text on this. Other criteria will be discussed in the sections below.

2.1.3 Particle Identification

In this analysis, the proton and pion selection are simply based on n_σ and DCA to primary vertex. The selected π has a purity of 100% at low p_T range, and proton purity is also high to 100% with $p_T \geq 1.1$ GeV/c. All detailed values are listed in figure 2.

When select deuteron, due to the lack of $n_{\sigma(d)}$, we introduce a new variable Z , which is defined as :

$$Z = \ln\left(\frac{dE}{dx}\right)_{data} - \ln\left(\frac{dE}{dx}\right)_{Bichsel} \quad (1)$$

This variable reflects the difference between the measured and theoretical value of energy loss.

	Run11 27GeV	Run10 39GeV	Run11 200GeV
Track Flag	(0,1000)	(0,1000)	(0,1000)
q	1	1	1
nHitsFit	≥ 25	> 25	≥ 25
nHitsDedx	≥ 15	> 15	≥ 15
n	< 1	< 1	< 1
Pt	> 0.2	> 0.2	> 0.2
nHitsFit/nHitsPoss	[0.52,1.02]	[0.52,1.02]	[0.52,1.02]
Deuteron charge	1	1	1
Deuteron z	< 0.2	< 0.2	< 0.1
Proton Charge	1	1	1
Proton Nol	< 2.0	< 2.0	< 2.0
Proton DCA	> 0.5	> 0.5	> 0.5
Pion Charge	-1	-1	-1
Pion Nol	< 2.0	< 2.0	< 2.0
Pion DCA	> 0.8	> 0.8	> 0.8
DCA 1-2	< 1.0	< 1.0	< 0.8
DCA 1-3	< 1.0	< 1.0	< 0.8
DCA 2-3	< 0.8	< 0.8	< 0.8
DCA 1-xv0123	< 1.2	< 1.2	< 1.0
DCA 2-xv0123	< 1.2	< 1.2	< 1.0
DCA 3-xv0123	< 1.2	< 1.2	< 1.0
(Virtual) \wedge DL	[2.4,150]	[2.4,150]	[2.4,150]
(Virtual) \wedge DCA	[0,0.9]	[0,1.0]	[0.6,1.6]
(Virtual) \wedge Angle	-	20	< 5
(Virtual) \wedge Mass	< 1.112	< 1.110	< 1.111
Hypertriton DL	[2.4,150]	[2.4,150]	[2.4,150]
Hypertriton DCA	< 1.0	< 1.0	< 0.6
Hypertriton Pt	> 3.0	> 3.0	> 3.0
Angle 1-2	-	-	≤ 20
Angle 1-3	-	-	≤ 40
Angle 2-3	-	-	≤ 40

(Virtual) Lambda Momentum	Proton DCA	Pion DCA
≤ 0.8	≥ 1.00	≥ 2.50
[0.8,3.6)	≥ 0.75	≥ 2.00
≥ 3.6	-	≥ 1.00

	Proton	Pion
TOF Beta	> 0	> 0
TOF LocalY	< 1.8	< 1.8
Mass Range	[0.5,1.3]	[0,0.3]

Figure 2: Detailed cuts applied in three body decay channel analysis. Including all PID cuts and topological cuts.

2.1.4 Signal Extraction

After the particle identification, we then extract the signal by applying other topological cuts mentioned in figure 2, including the DCA between daughters, DCA of daughters to PV, decay length of signal candidate, and so on. Those cuts are optimized separately for different energies.

Especially, in order to enhance the signal to background ratio, we use the proton and pion pair to form a (virtual) Λ , and require the invariant mass the $p - \pi$ pair to be slightly smaller than a real Λ . This will reject a large amount of background from Λ decays.

2.2 Two Body Part

Bad runs listed in StRefMultCorr have been excluded. Additional run by run QA on several parameters has been done and some abnormal runs are excluded. The statistics I show below are all obtained after all bad runs are excluded.

Figure 3 to Figure ?? are run by QA plots for bad run exclusion.

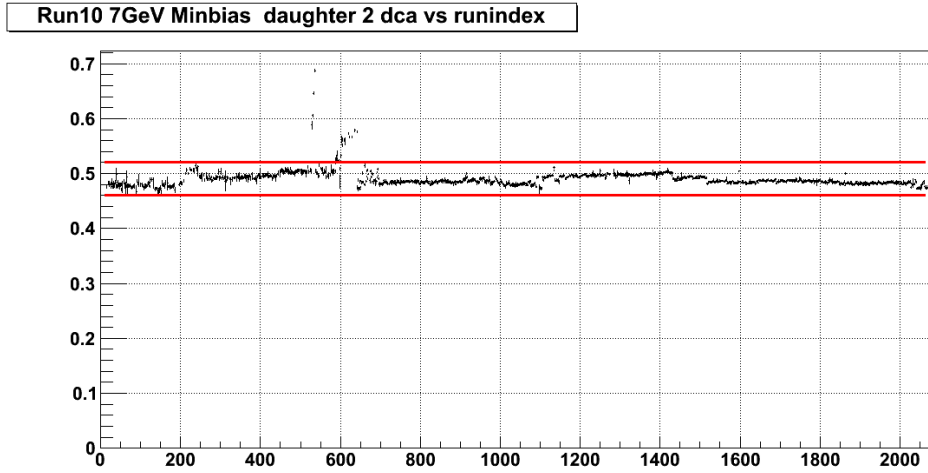


Figure 3: Run10 7GeV minimum biased data π^- DCA vs run index. The two red lines indicate the rejection zone.

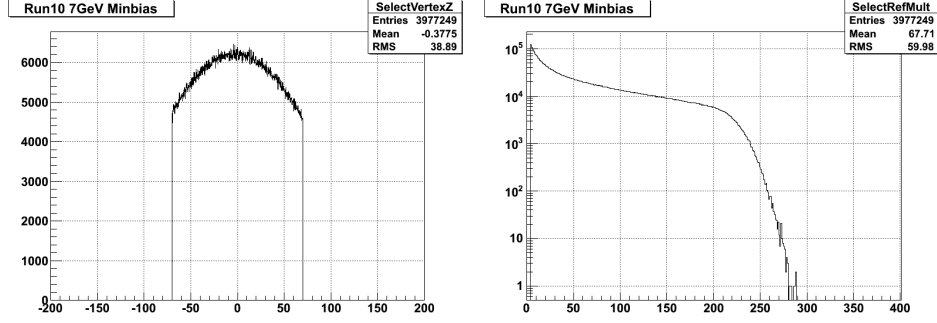


Figure 4: Run10 7 GeV data. The vertex Z and reference multiplicity distribution of selected events.

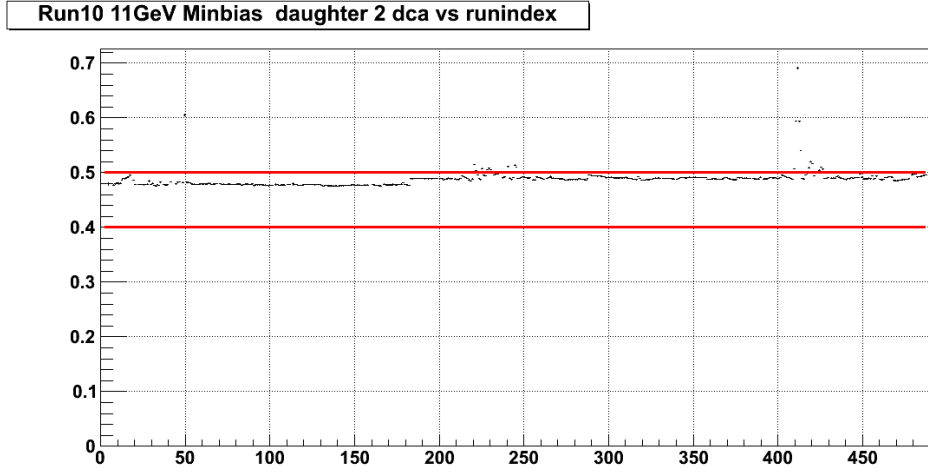


Figure 5: Run10 11GeV minimum biased data π^- DCA vs run index. The two red lines indicate the rejection zone.

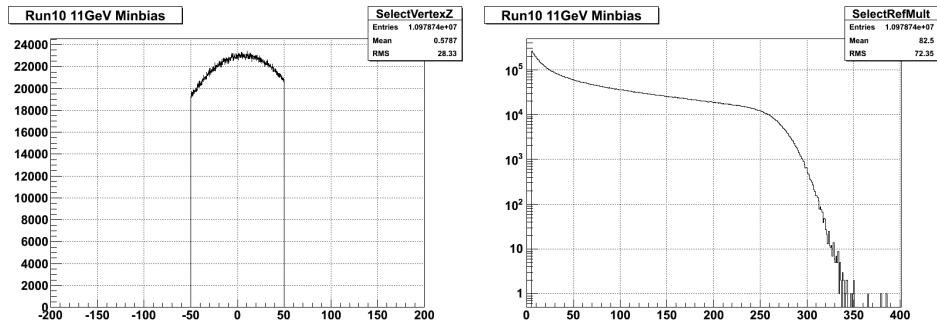


Figure 6: Run11 11GeV data. The vertex Z and reference multiplicity distribution of selected events.

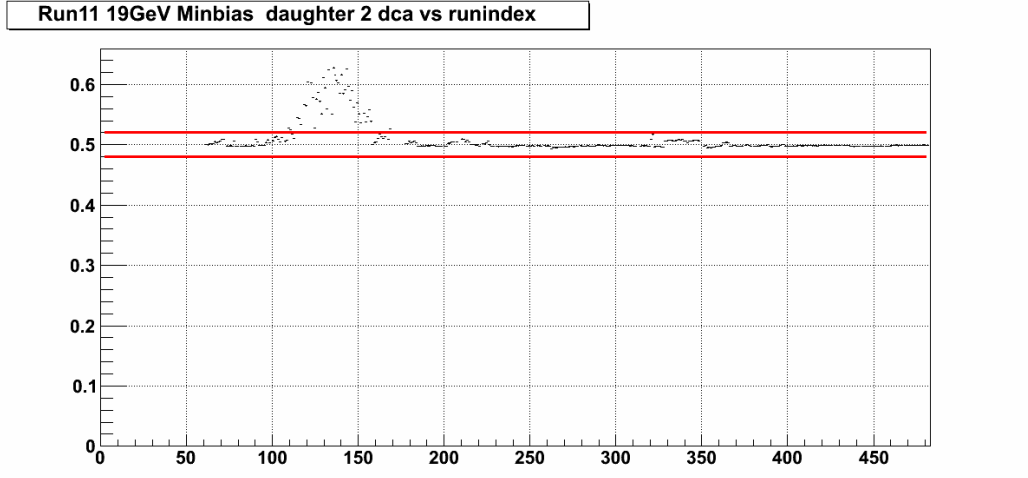


Figure 7: Run11 19GeV minimum biased data π^- DCA vs run index. The two red lines indicate the rejection zone.

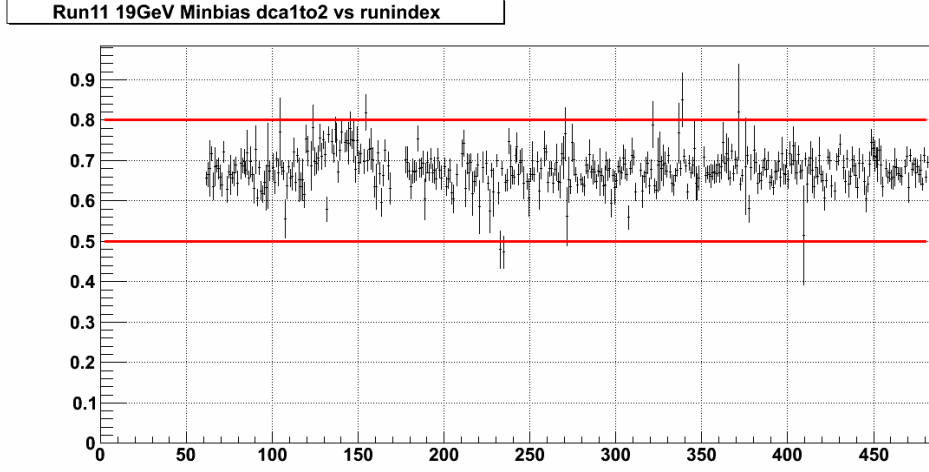


Figure 8: Run11 19GeV minimum biased data. DCA of ${}^3\text{He}$ to π^- vs run index. The two red lines indicate the rejection zone.

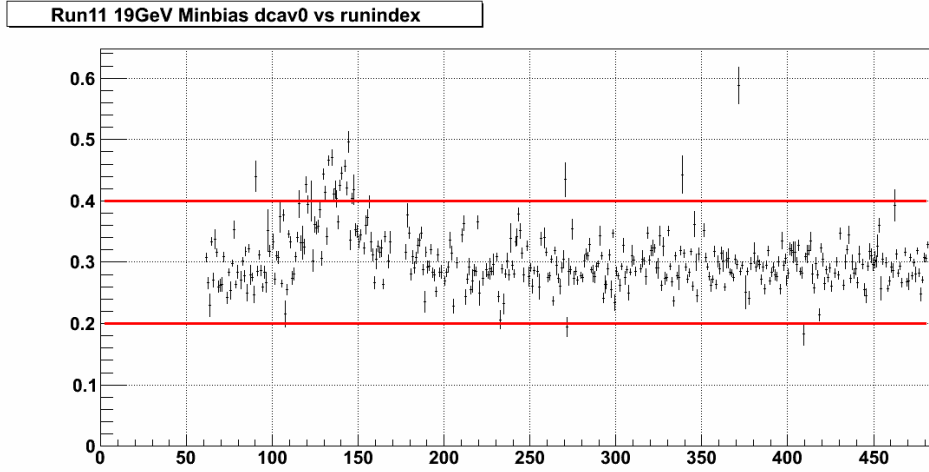


Figure 9: Run11 19GeV minimum biased data. DCA of v^0 vs run index. The two red lines indicate the rejection zone.

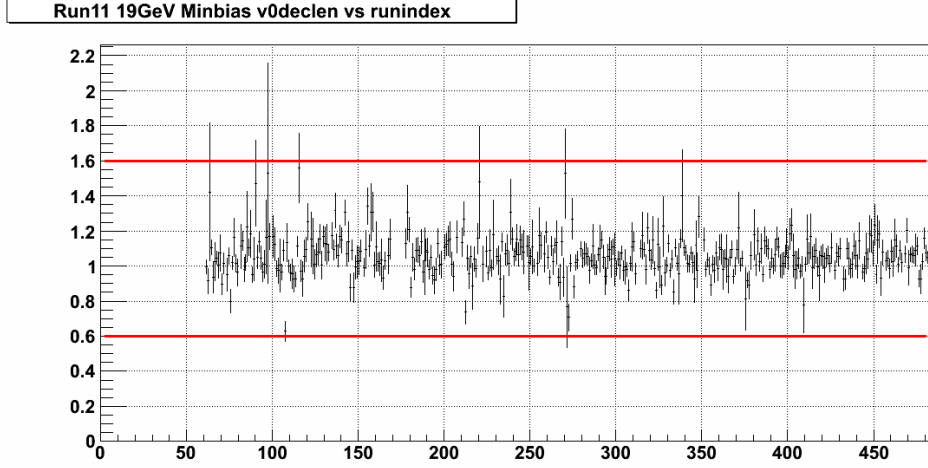


Figure 10: Run11 19GeV minimum biased data. Decay length of v^0 vs run index. The two red lines indicate the rejection zone.

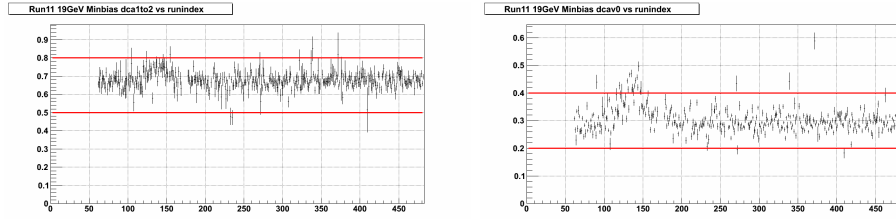


Figure 11: Run11 19GeV data. The vertex Z and reference multiplicity distribution of selected events.

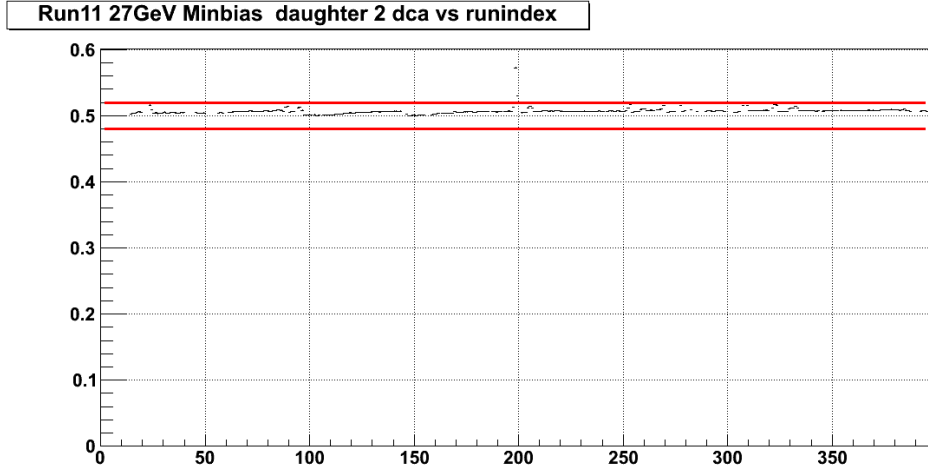


Figure 12: Run11 27GeV minimum biased data. DCA of v^0 vs run index. The two red lines indicate the rejection zone.

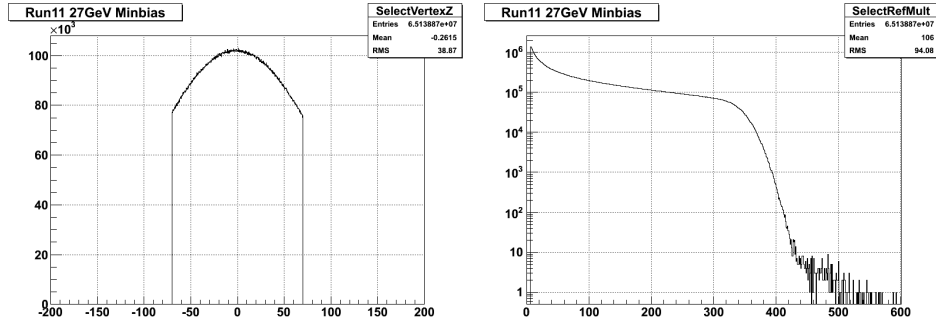


Figure 13: Run11 27GeV data. The vertex Z and reference multiplicity distribution of selected events.

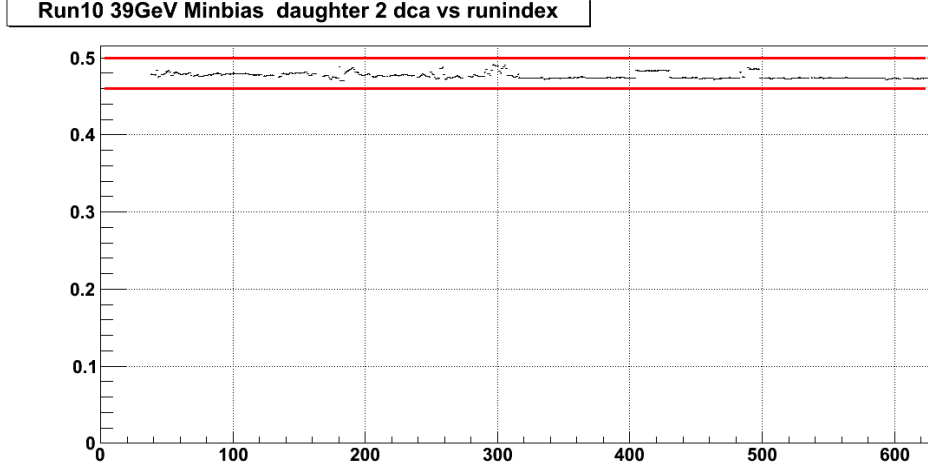


Figure 14: Run10 39GeV minimum biased data π^- DCA vs run index. The two red lines indicate the rejection zone.

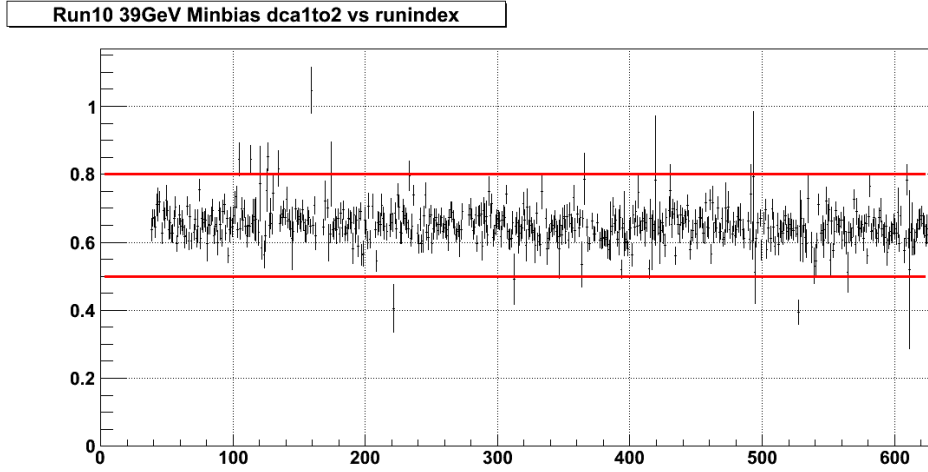


Figure 15: Run10 39GeV minimum biased data. DCA of ${}^3\text{He}$ to π^- vs run index. The two red lines indicate the rejection zone.

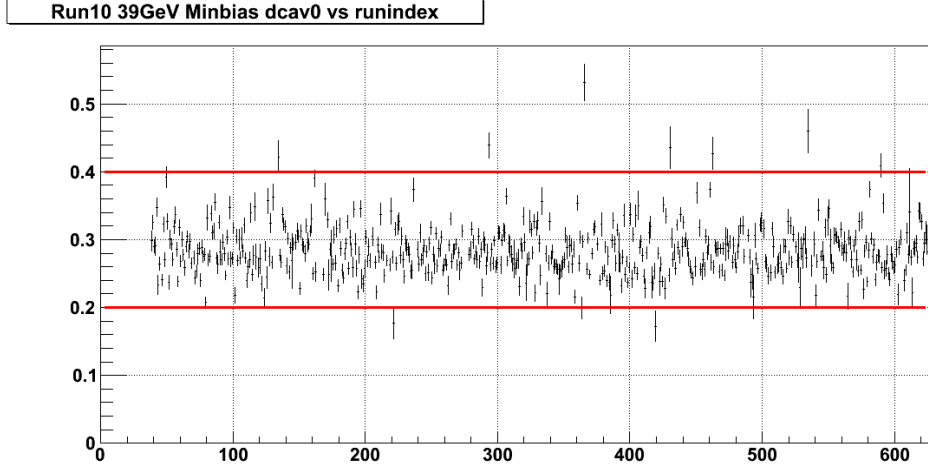


Figure 16: Run10 39GeV minimum biased data. DCA of v^0 vs run index. The two red lines indicate the rejection zone.

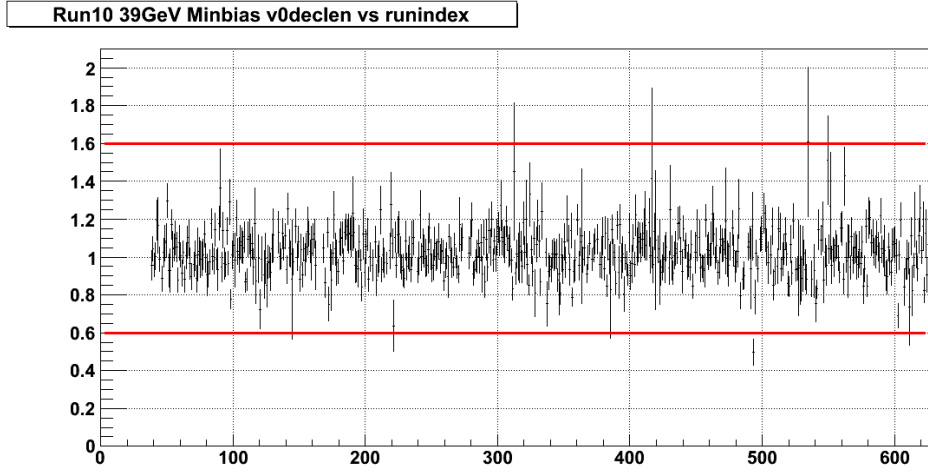


Figure 17: Run10 39GeV minimum biased data. Decay length of v^0 vs run index. The two red lines indicate the rejection zone.

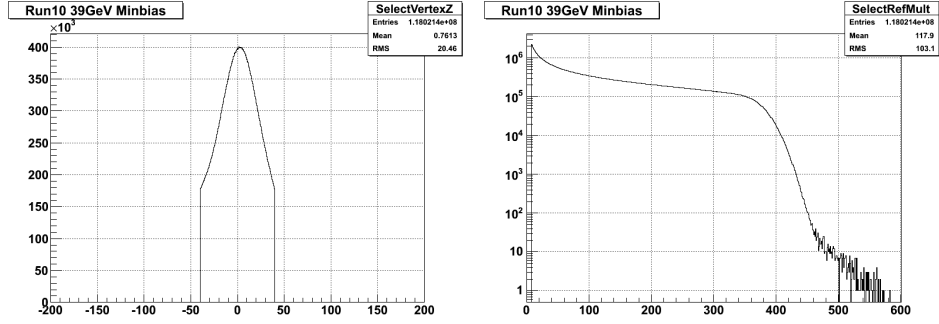


Figure 18: Run10 39GeV data. The vertex Z and reference multiplicity distribution of selected events.

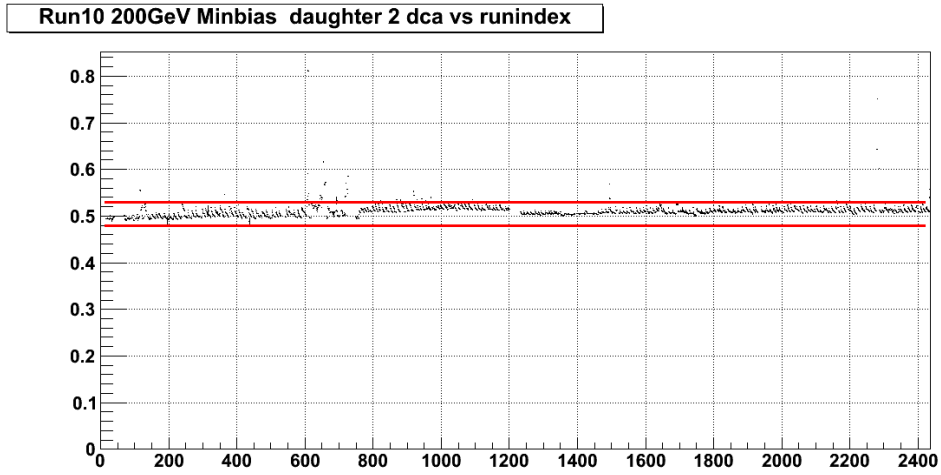


Figure 19: Run10 200GeV minimum biased data π^- DCA vs run index. The two red lines indicate the rejection zone.

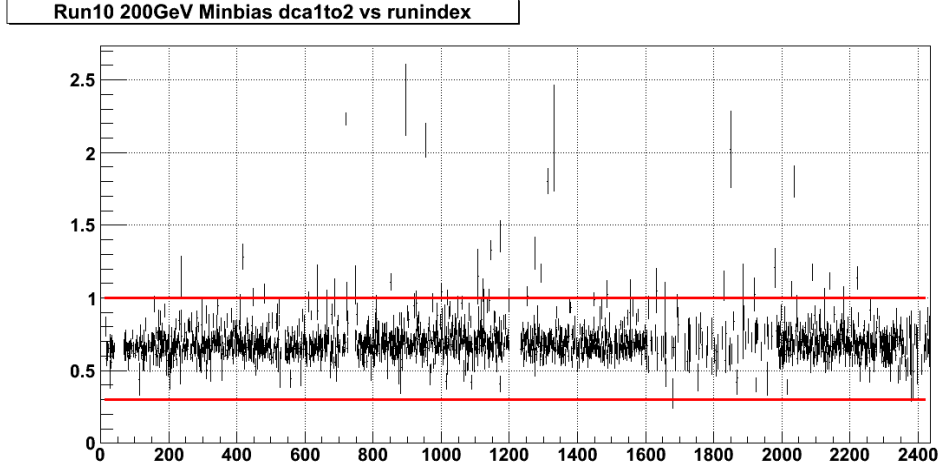


Figure 20: Run10 200GeV minimum biased data. DCA of 3He to π^- vs run index. The two red lines indicate the rejection zone.

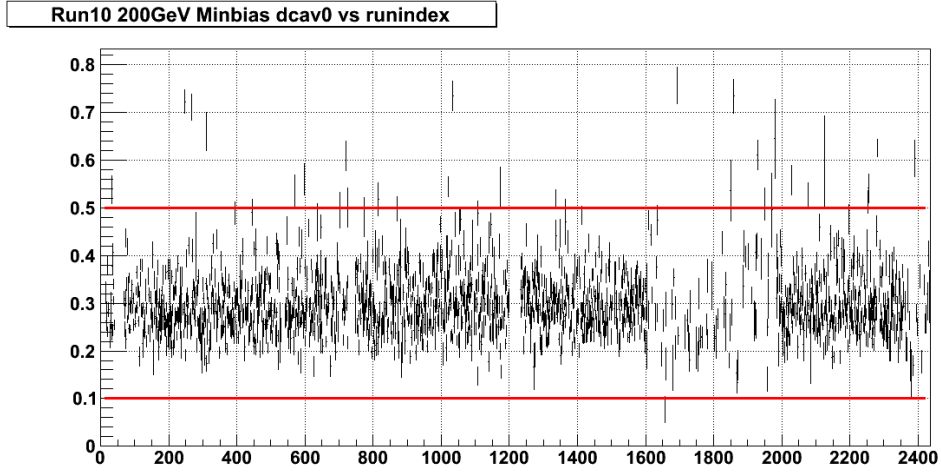


Figure 21: Run10 200GeV minimum biased data. DCA of ν^0 vs run index. The two red lines indicate the rejection zone.

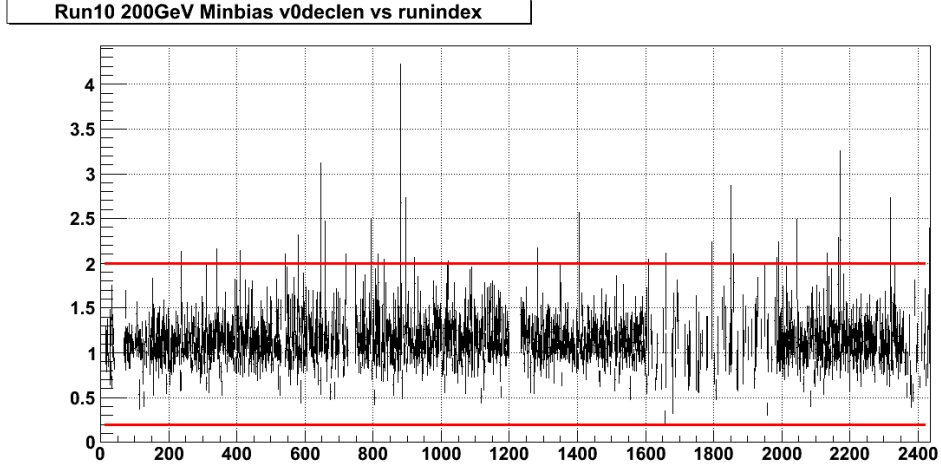


Figure 22: Run10 200GeV minimum biased data. Decay length of v^0 vs run index. The two red lines indicate the rejection zone.

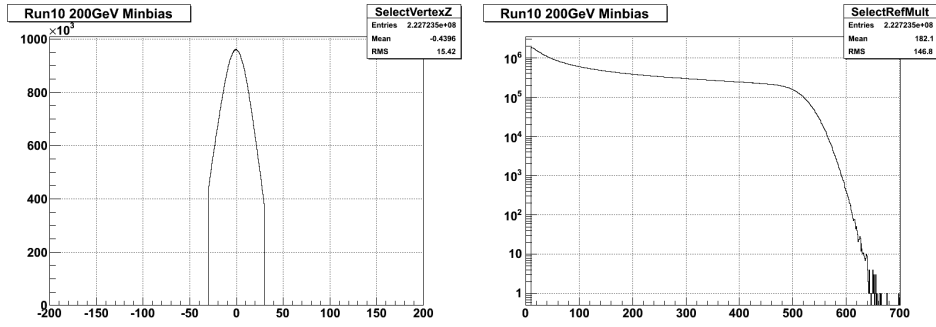


Figure 23: Run10 200GeV data. The vertex Z and reference multiplicity distribution of selected events.

2.2.1 Event-level cuts and statistics

The event-level cuts and statistics as well as track-level cuts are as shown in figure 24 and figure 25.

Run-10 Au+Au 7.7 GeV	MB trigger~3.98M events	vz < 70cm	Refmult(Hiroshi StRefMultCorr)
Run-10 Au+Au 11.5 GeV	MB trigger~10.98M events	vz < 50cm	Refmult(Hiroshi StRefMultCorr)
Run-11 Au+Au 19.6 GeV	MB trigger~31.15M events	vz < 70cm	Refmult(Hiroshi StRefMultCorr)
Run-11 Au+Au 27 GeV	MB trigger~48.65 events	vz < 50cm	Refmult(Hiroshi StRefMultCorr)
Run-10 Au+Au 39 GeV	MB trigger~118.02M events	vz < 40cm	Refmult(Hiroshi StRefMultCorr)
Run-10 Au+Au 200 GeV	MB trigger~222.73M events	vz < 30cm; Vpdvz-vz < 4cm	Refmult(Hiroshi StRefMultCorr)
Run-10 Au+Au 200 GeV	Central trigger~199.07M events	vz < 30cm	Refmult(Hiroshi StRefMultCorr)
Run-7 Au+Au 200 GeV	MB trigger~56.31M events	vz < 30cm	Refmult ≥ 10

Figure 24: event level cuts and statistics for two body analysis.

NHitsFit(TPC)	≥ 25
NHitsdEdx	≥ 15
NHitsFit/NMaxs	$>0.52 \ \&\& \ <1.02$
letal	<1.0
pt	$>0.20\text{GeV}$

Figure 25: track level basic cuts for two body analysis.

2.2.2 ^3He PID

STAR TPC is able to identify charge particles including π, K, p, d and ^3He , *et al.*, via recoding their ionization energy loss (dE/dx) during their travel in the TPC. The amount of ionization energy loss in the TPC depends on the particle's velocity and charge. Since the dE/dx distribution for a fixed particle type is not Gaussian, here we use a new variable:

$$Z = \ln\left(\frac{dE}{dx}\right)^{data} - \ln\left(\frac{dE}{dx}\right)^{Bichsel} \quad (2)$$

to properly deconvolute the distributions into Gaussians.

In order to identify ^3He , we require $DCA < 1\text{cm}$, $rigidity > 1\text{GeV}/c$ and $Z(-0.2, 0.2)$. We can see from the Z distribution below that He3 can be identified cleanly using the above cuts.

As we use six different energies in this analysis, the ^3He identification are shown individually in the figure 27. Identified ^3He statistics are listed in the figure 28.

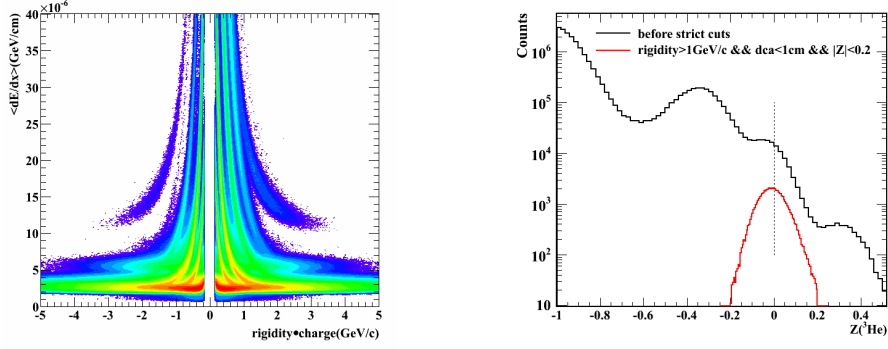


Figure 26: Left panel is dE/dx distribution for all particles. Right panel is ${}^3\text{He}$ identification with detailed cuts. We can see that the Z distribution of ${}^3\text{He}$ is quite clean after cuts.

2.2.3 π PID

We do not do precise π identification. In this analysis, a cut $|n_\sigma| < 2$ is applied to get daughter 2.

2.2.4 Signal Extraction

This picture shows the secondary vertex finding technique adopted in this analysis. The V0 topology of the two-body decay and the relative V0 parameters are demonstrated in the figure 1 too. In figure 29, we listed the detailed topological cuts.

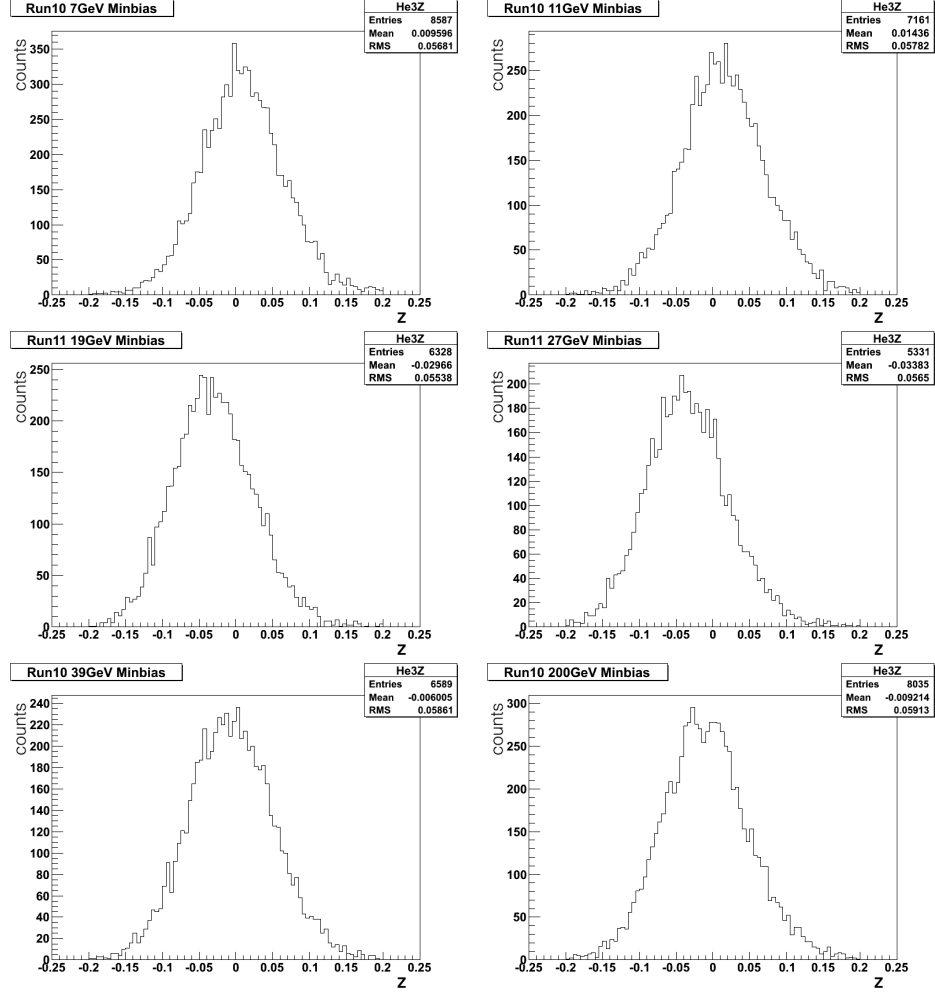


Figure 27: ^3He identification plots at separate energies. The x-axis is Z distribution, the y-axis represents counts of ^3He .

Data Set	He3	antiHe3
Run-10 Au+Au 7.7 GeV Minbias	8587	0
Run-10 Au+Au 11.5 GeV Minbias	7161	0
Run-11 Au+Au 19.6 GeV Minbias	6321	7
Run-11 Au+Au 27 GeV Minbias	5312	19
Run-10 Au+Au 39 GeV Minbias	6456	133
Run-10 Au+Au 200 GeV Minbias	5822	2213
Run-10 Au+Au 200 GeV Central	11181	4241
Run-7 Au+Au 200 GeV Minbias	2264	861

Figure 28: identified ^3He statistics at separate energies in two body analysis.

V0 Cuts	Run10 7.7GeV	Run10 11.5GeV	Run10 39GeV	Run11 19.6GeV	Run11 27GeV	Run10 200GeV minbias	Run10 200GeV central	Run7 200GeV
DCA from daughter1 to daughter2	<1.0cm	<0.8cm	<1.0cm	<0.9cm	<1.0cm	<0.8cm	<1.0cm	<1.0cm
Distance of Closest Approach (DCA) from the v0 candidate to the primary vertex	<1.0cm	<0.8cm	<0.9cm	<1.0cm	<1.0cm	<1.0cm	<1.1cm	<1.0cm
v0 candidate decay length	>2.4cm	>2.1cm	>2.0cm	>3.8cm	>3.5cm	>3.3cm	>2.6cm	>2.4cm
DCA from π candidate to primary vertex	>0.9cm	>0.8cm	>0.7cm	>1.2cm	>1.0cm	>1.0cm	>0.9cm	>0.8cm

Figure 29: $^3\Lambda$ H two body decay topological cuts. All are optimized separately for different energies.

3 ${}^3_\Lambda\text{H}$ signal

3.1 Three Body Part

3.1.1 Invariant Mass

The hyper triton signal is shown via invariant mass plots in figure 32. In this figure, the upper left panel is the invariant mass distribution from Run11 27GeV data, the upper right panel is Run10 39GeV data, the lower left one is Run11 200GeV data, and the lower right panel is the combined result. In all panels, the red dots are the signal with background distribution, and the black histogram is the background distribution. The background is derived by rotating a deuteron by 180 degree with respect to the primary vertex in the azimuthal plane. The background and signal distributions are fitted in order to get a intuitional feeling about the peak position and signal counts. The fitting function for background and signal is shown in equation 3 and 4.

$$f_{bkg}(x) = p_0(e^{-\frac{x-p_3}{p_1}} - e^{-\frac{x-p_3}{p_2}}) + p_4 \quad (3)$$

$$f_{sig}(x) = f_{bkg}(x) + gauss(x) \quad (4)$$

3.1.2 Signal Counts

The ${}^3_\Lambda\text{H}$ decays obey the decay law:

$$N(t) = N_0 e^{-t/\tau} = N_0 e^{-\ell/\beta\gamma c\tau} \quad (5)$$

where ℓ is the ${}^3_\Lambda\text{H}$ decay length. $\beta = v/c$, $\gamma = \frac{1}{\sqrt{1-\beta^2}}$, τ is the lifetime and c is the speed of light. Here ℓ could be derived by reconstruct primary and secondary vertex. From the four momentum of hypertriton signal, we can calculate γ and β of it. So we can calculate the lifetime by fitting the $\ell/\beta\gamma$ distribution of ${}^3_\Lambda\text{H}$. Here $\ell/\beta\gamma$ could be derived by using measured decay length of signal to be divided by the γ and β of particle.

As the number of hyper triton are quite limited, we use only 3 $\ell/\beta\gamma$ bins: [2.4, 8] cm, [8, 13] cm, and [13, 25] cm. We use equation ?? to fit the background and use equation 4 to fit the signal. Then, for each bin, signal data point with statistical error is used for signal counting. For background, in order to reduce error, we use fitted background value for signal counts. For example, if in one bin, the signal counts are $N_{sig} \pm E_{sig}$, and the fitted background is $N_{bkg} \pm E_{bkg}$, we set E_{bkg} to be zero, and use $N_{sig} \pm E_{sig}$ minus $N_{bkg} \pm 0$ as signal count. The number of hyper triton in each bin is derived by using value of data point minus fitting value of background.

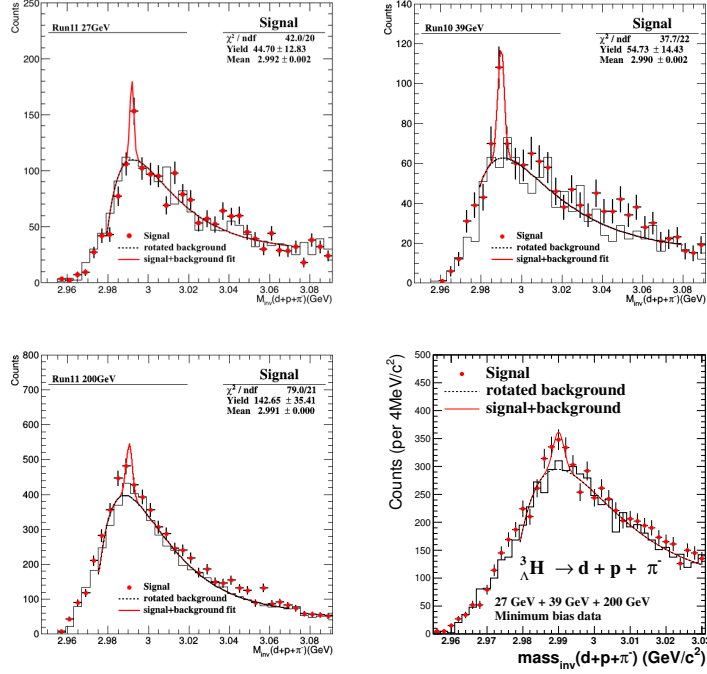


Figure 30: Invariant mass of ${}^3_{\Lambda}\text{H}$. The upper left and right panels are 27GeV and 39GeV data, the lower panels are 200GeV data and combined data.

The fitting results are shown in figure 31 below. In this figure, the upper left panel is combined result, the upper right panel is the invariant mass distribution of first $\ell/\beta\gamma$ bin, the lower two panels are second and third bins. The green band indicate the signal region. And the χ^2 values are also shown in each panel. The ${}^3_{\Lambda}\text{H}$ counts in each bin is: 74.83 ± 25.67 , 66.89 ± 22.47 and 36.00 ± 12.49 .

3.2 Two Body Part

Please note: in two body part of this analysis, hypertriton and antihypertriton signals are combined together.

3.2.1 Signal and background counting

The background is reconstructed via rotating one of the daughter candidates with a specific angle with respect to the event primary vertex in the azimuthal plane. In our analysis, we rotate the 180 degrees. We fit the background distribution with a double exponential function.

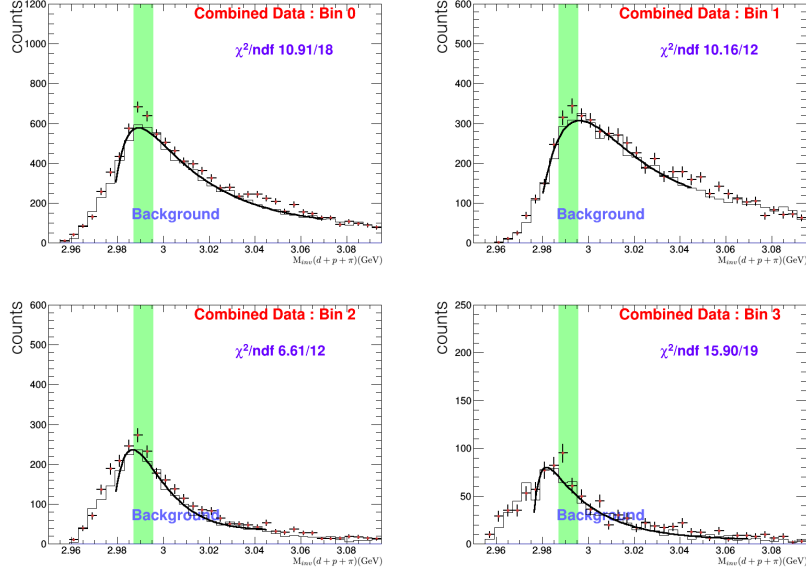


Figure 31: Signal counts in each $\ell/\beta\gamma$ bin. the upper left panel is combined result, the upper right panel is the invariant mass distribution of first $\ell/\beta\gamma$ bin, the lower two panels are second and third bins. The green band indicate the signal region.

Below shows the combined ${}^3_{\Lambda}\text{H} + {}^3_{\Lambda}\overline{\text{H}}$ invariant mass spectra using all the datasets analyzed. The signal is very clean and has a significance of 9.53σ . Therefore, we constrain a fixed mass window for counting the signal: 2.986 - 2.996 GeV.

3.2.2 Signals reconstructed in separate datasets

The signal is calculated via bin-bin counting in the fixed mass range 2.986 to 2.996 GeV with fitted background subtraction. The ${}^3_{\Lambda}\text{H}$ invariant mass distribution at separate energy is shown in figure 33.

3.2.3 Combined Signal QA

In order to check the signals reconstructed at each dataset are reliable, we combine some of the results and fit the signal, as demonstrated in figure 34

The combined signals have consistent counts with separate signals, so I can conclude that the separate signals are reliable.

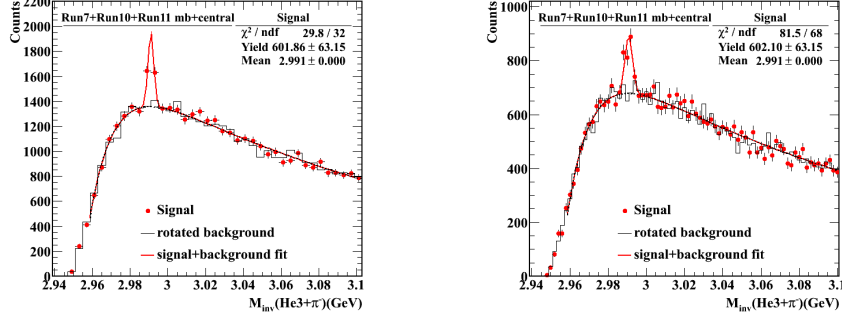


Figure 32: ${}^3_{\Lambda}\text{H}$ two body channel invariant mass distribution. Left panel is with 4 MeV bin width, the right panel is with 2 MeV bin width.

3.2.4 Signal Counts

Let's start from the radioactive decay raw:

$$N(t) = N_0 e^{-t/\tau} = N_0 e^{-\ell/\beta\gamma c\tau} \quad (6)$$

by analyzing the yield in different $c\tau$ bins, one can extract the lifetime parameter. Below we show the hypertriton signal in 4 decay bins($\ell/\beta\gamma$) from left to right: $[2.0, 5.0]$, $[5.0, 8.0]$, $[8.0, 11.0]$, $[11.0, 101.0]$.

The ${}^3_{\Lambda}\text{H}$ yields in different $\ell/\beta\gamma$ bins is shown in figure 35. Considering the counts of ${}^3_{\Lambda}\text{H}$ in two body analysis, we use four $\ell/\beta\gamma$ bins here.

Finally, we use the same method to fit the data points as used in three body analysis. The result is shown in figure 36. The lifetime from two body analysis is 123^{+26}_{-22} (stat.) .

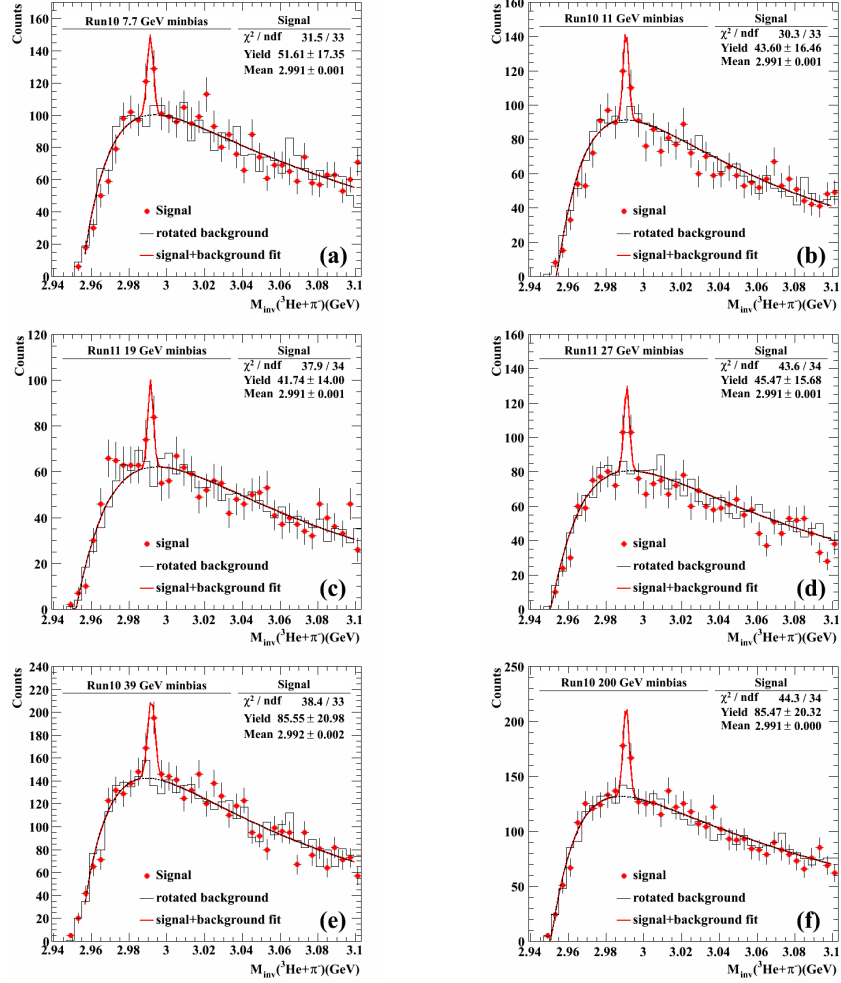


Figure 33: ^3He identification plots at separate energies. The x-axis is Z distribution, the y-axis represents counts of ^3He .

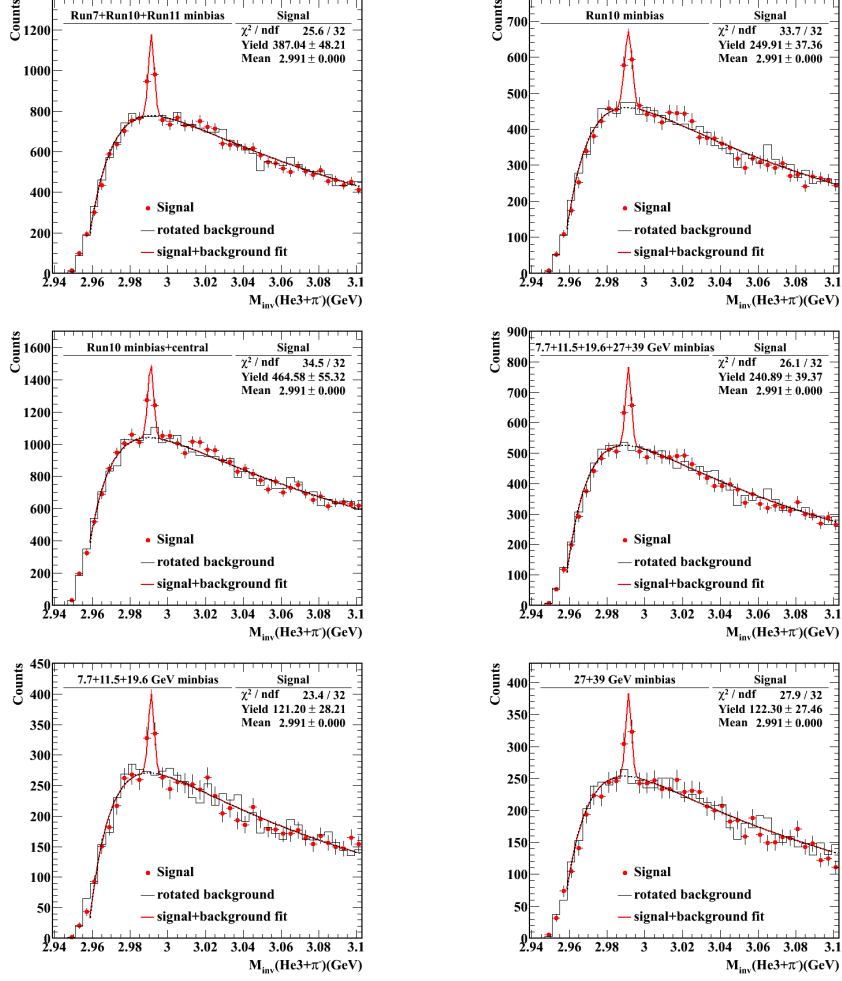


Figure 34: ${}^3_{\Lambda}\text{H}$ invariant mass QA plots. We tried to add different energies to shown invariant mass and ${}^3_{\Lambda}\text{H}$ counts in order to prove reliability of the analysis.

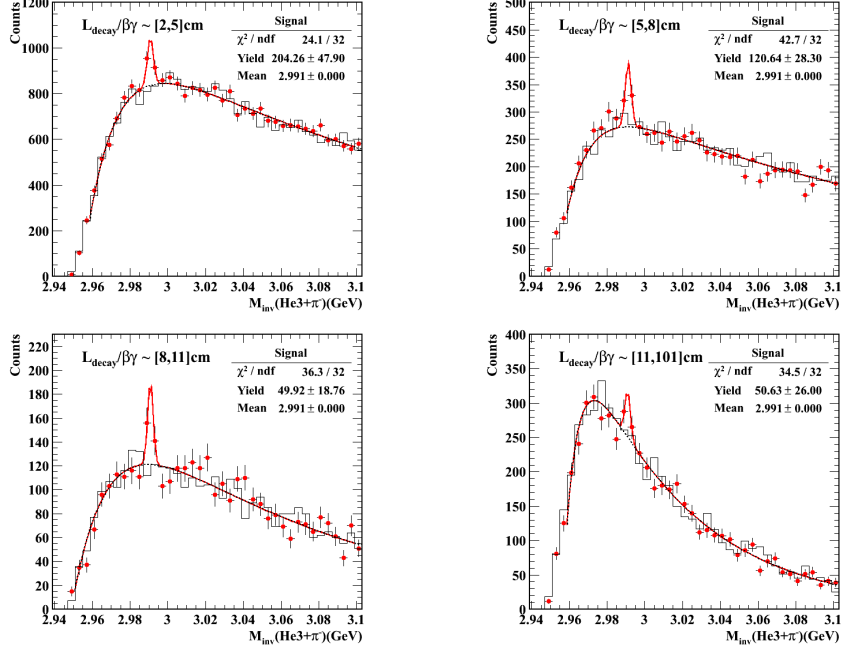


Figure 35: ${}^3\text{H}$ yields in four different $\ell/\beta\gamma$ bins. The upper left panel indicates the $\ell/\beta\gamma$ [2.0,5.0], the upper right panel is $\ell/\beta\gamma$ [5.0,8.0], the lower left panel is $\ell/\beta\gamma$ [8.0,11.0] and lower right panel is $\ell/\beta\gamma$ [11.0,101.0].

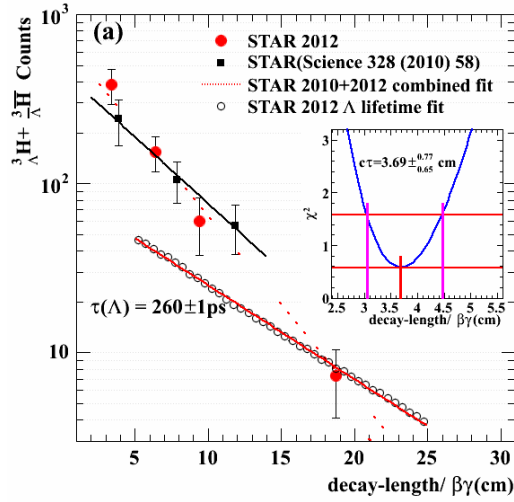


Figure 36: lifetime fit for two body analysis.

4 Embedding

4.1 Three Body Part

Due to the limited tracking efficiency and acceptance of STAR detectors, we need to correct the ${}^3_\Lambda\text{H}$ yield. We required embedding data for these energies. The whole embedding analysis procedure is shown in figure 37. After read an event, we applied exactly the same cuts as used in data analysis except for those PID cuts. Then we record the numbers of Monto-Carlo ${}^3_\Lambda\text{H}$ in each $\ell/\beta\gamma$ bin, and calculate the efficiency in the end with binomial errors. The efficiencies for each energy in each $\ell/\beta\gamma$ bins are shown in figure 38 below.

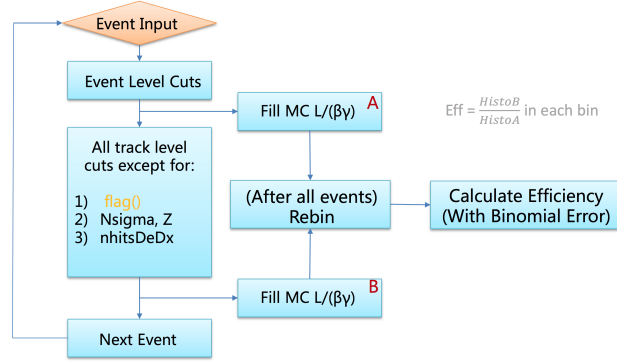


Figure 37: Embedding analysis flow chart. The cuts used for ${}^3_\Lambda\text{H}$ reconstruction is exactly the same except for PID cuts.

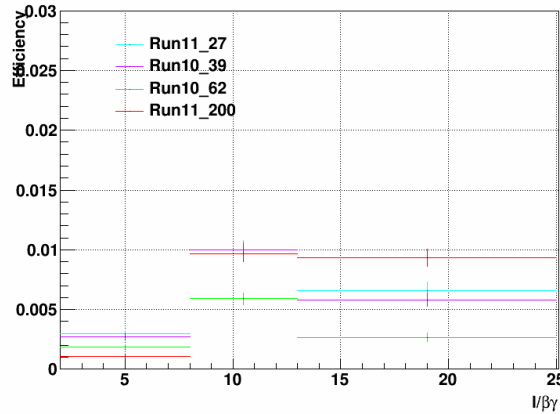


Figure 38: Signal counts efficiency in each $\ell/\beta\gamma$ bin for different energies. Different colors indicate different energies.

Then the efficiency in each bin is then combined with function 7.

$$\epsilon_i = \frac{N_{ev27}(\frac{dN}{dy})\epsilon_{27-i} + N_{ev39}(\frac{dN}{dy})\epsilon_{39-i} + N_{ev200}(\frac{dN}{dy})\epsilon_{200-i}}{N_{ev27}(\frac{dN}{dy}) + N_{ev39}(\frac{dN}{dy}) + N_{ev200}(\frac{dN}{dy})} \quad (7)$$

where ϵ_i indicates the combined efficiency for i bin, $\frac{dN}{dy}$ is the invariant yield of ${}^3\text{He}$. (Here we use ${}^3\text{He}$ yield for calculation due to the lack of accurate ${}^3_\Lambda\text{H}$ yield.) With efficiency derived above, we can calculate the ${}^3_\Lambda\text{H}$ yield in each $\ell/\beta\gamma$ bin. The signal counts, combined efficiency and the invariant yield of ${}^3_\Lambda\text{H}$ is shown in figure 39.

	Signal Counts	Efficiency (%)	Yield
[2,4,8)	74.83±25.67	0.36±0.01	20605±7085
[8,13)	66.89±22.47	1.36±0.03	4917±1655
[13,25)	36.00±12.49	0.81±0.02	4428±1541

Figure 39: Signal counts, combined efficiency and invariant yield of ${}^3_\Lambda\text{H}$ in each $\ell/\beta\gamma$ bin.

4.2 Two Body Part

4.2.1 Embedding QA

I incorrectly requested distribution should be flat in $[-1,1]$, instead of y . As shown in figure 40.

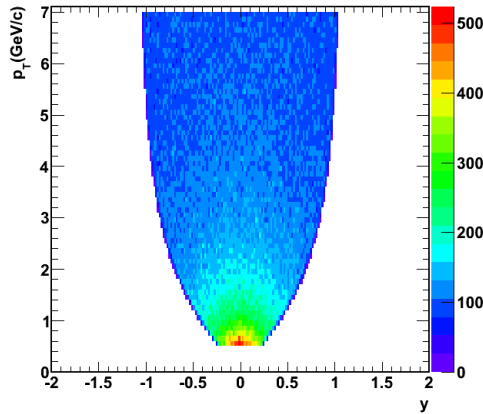


Figure 40: The input y distribution in two body embedding analysis.

4.2.2 Embedding Rapidity Correction

In order to get the correct efficiency, I need to correct two issues: 1. Ununiform y distribution in a certain p_T bin; 2. Decreased y gap in a certain p_T bin due to the $\eta[-1,1]$ cut.

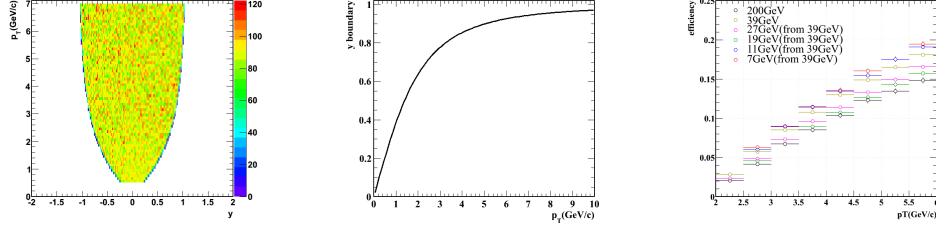


Figure 41: Left panel: p_T vs y distribution after rapidity distribution corrected to be flat. Middle panel: rapidity gap vs p_T after $\eta[-1,1]$ cut is applied. Right panel: ^3H efficiency vs p_T after rapidity distribution corrected.

Figure 42 shows the comparison of several V0 parameters of data and simulation(with different pT weight) using Run10 200GeV embedding sample.

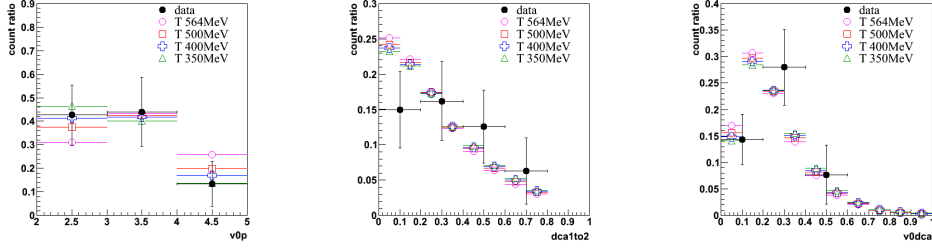


Figure 42: Comparison of several different V0 parameters of data and simulation. This shows the different when using different parameters for efficiency calculation.

The efficiency of the other energies are extrapolated from 200GeV embedding sample by weighting Vz and reference multiplicity distribution.

4.2.3 Efficiency

The final efficiency for two body ${}^3\Lambda\text{H}$ analysis is shown in figure 43. From the efficiency, we can use combined datasets to calculate lifetime.

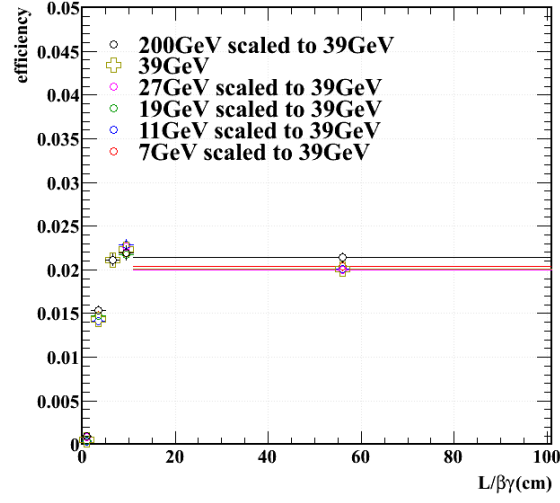


Figure 43: Efficiency in four $\ell/\beta\gamma$ bins.

5 Lifetime Analysis

The decay of hyper triton obeys the particle decay law, we can use the hyper triton yield with $\ell/\beta\gamma$ to calculate the lifetime of hyper triton. As the ratio (B.R.(2-body)/B.R.(3-body)) will also be calculated, we now will correct the number of events by yields. (So the two channels will have same N_0 in decay law function.)

Because the ${}^3_{\Lambda}\text{H}$ yield is small and with large error, meanwhile the ${}^3\text{He}$ yield is proportional to hyper triton and is much preciser. We will use ${}^3\text{He}$ yield to correct number of events for ${}^3_{\Lambda}\text{H}$. The event number correction details are listed in figure 44 and figure 45. In figure 44 we listed the ${}^3\text{He}$ counts, efficiency, number of events used and final invariant yield. In figure 45 we show the scaled number of events with respect to 39 GeV data. So we can see that, the 2-body and 3-body analyses are using 724.89 million and 579.98 million equivalent 39GeV events, respectively.

	Counts	Efficiency	Event #	Helium-3 Yield (M)
Run10 7.7	8587	0.423	3.98	5101
Run10 11.5	7161	0.426	10.98	1531
Run11 19.6	6321	0.403	31.15	504
Run11 27	5312	0.402	48.65	272
Run10 39	6456	0.407	118.02	134
Run11 200	5822	0.424	222.73	62

Figure 44: Detailed ${}^3\text{He}$ information for this analysis. Including ${}^3\text{He}$ counts, reconstruction efficiency, number of events used and, finally, the ${}^3\text{He}$ yields in different energies.

With corrected yield, we fit the data points with decay lay function and then use minimum χ^2 method for estimation of lifetime. The result is 142^{+24}_{-21} (stat.) ps. Figure 46 shows the fitting result and χ^2 distribution.

	2-body		3-body	
	Event #	Scaled #	Event #	Scaled #
Run10 11.5	10.98 M	125.37 M		
Run11 19.6	31.15 M	117.16 M		
Run11 27	48.65 M	98.75 M	53.31 M	108.21 M
Run10 39	118.02 M	118.02 M	134.41 M	134.41 M
Run10 200	222.73 M	102.39 M	516.87 M	237.61 M
Total	435.51 M	713.20 M	704.59 M	480.23 M

Figure 45: Event number correction for different energies for 2-body and 3-body analysis. The number is scaled to 39GeV data. i.e. for three body, 53.31 M 27 GeV data is equivalent to 108.21 M 39 GeV data in yield.

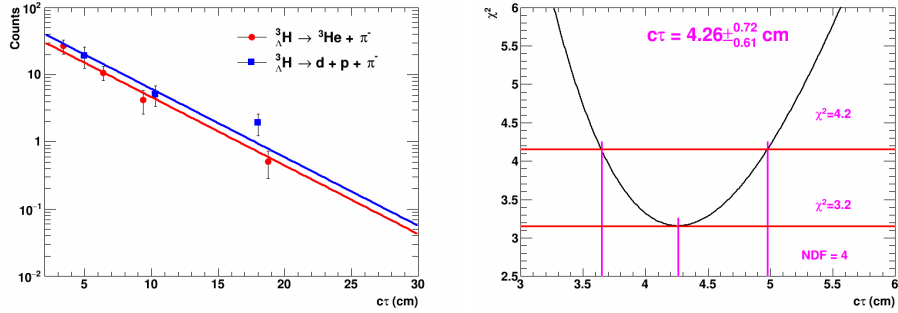


Figure 46: The combined lifetime fitting and the χ^2 distribution with $c\tau$. In left panel, the number of ${}^3_{\Lambda}\text{H}$ is already divided by theoretical branching ratio.

6 Ratio Analysis

As we can reconstruct hyper triton with both its 2-body and 3-body channels, its possible to measure the ratio of two branching ratios. Here we define:

$$\text{Ratio} = \frac{N_0 \times \text{B.R.}_{2\text{-body}}}{N_0 \times \text{B.R.}_{2\text{-body}} + N_0 \times \text{B.R.}_{3\text{-body}}} \quad (8)$$

This definition is different from a more commonly used variable, R_3 , which is defined as:

$$R_3 = \frac{\text{B.R.}_{2\text{-body}}}{\text{B.R.}_{\text{all mesonic decay}}} \quad (9)$$

however, considering that, theoretically, the sum of B.R.s of 2-body and 3-body channels is over 99% [11], the difference between R_3 and ratio would be small.

After correct the number of events used for 2-body and 3-body analysis, the fitting parameter N_0 are the same. So the ratio could be calculated as 0.32 ± 0.05 (stat.).

Table 2 summarizes previous measurements of this decay branching ratio in the literature. The present result is close to the combined measurement from helium bubble chamber experiments and is consistent with the average value of 0.35 ± 0.04 based on early measurements.

Table 2: Measurements of variable R_3 .

R_3	Technique	Ref.
0.39 ± 0.07	helium bubble chamber	[14]
$0.36^{+0.08}_{-0.06}$	helium bubble chamber	[16]
$0.39^{+0.12}_{-0.07}$	emulsion	[32]
$0.41^{+0.04}_{-0.03}$ to $0.46^{+0.04}_{-0.03}$	emulsion	[33]
0.30 ± 0.07	helium bubble chamber	[20]
0.35 ± 0.04	mean of helium bubble chamber results	[20]
0.32 ± 0.05	time projection chamber	this measurement

7 Systematic Uncertainty

7.1 Three Body Part

Here we take several kinds of contributions into account of systematic uncertainty:

- * Binning effect,
- * DCA between proton and pion
- * DCA of virtual lambda to primary vertex
- * Other sources

7.1.1 Binning Effect

For Binning effect, we change the bin width from 4MeV to 2MeV. Basic QA figures are shown below. Bin-0 is combination of all three bins. Bin-1 is $\ell/\beta\gamma$ [2,8], Bin-2 is $\ell/\beta\gamma$ [8,13] and Bin-3 is $\ell/\beta\gamma$ [13,25]. The signal counts are shown in table below. Figure 6 shows the hyper triton invariant mass in different $\ell/\beta\gamma$ bins. The uncertainty from binning is 8.76%.

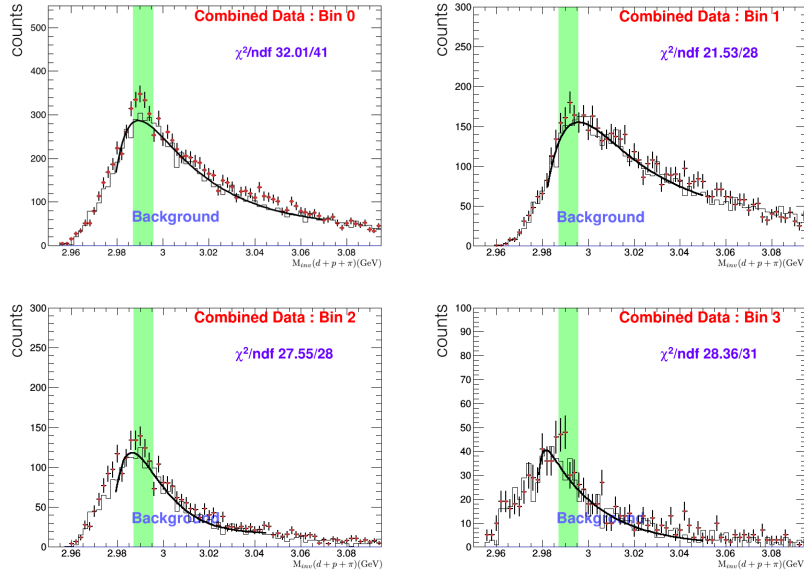


Figure 47: Invariant mass of ${}^3_{\Lambda}\text{H}$ in systematic uncertainty analysis from source : binning effect. Bin-0 is combination of all three bins. Bin-1 is $\ell/\beta\gamma$ [2,8], Bin-2 is $\ell/\beta\gamma$ [8,13] and Bin-3 is $\ell/\beta\gamma$ [13,25].

7.1.2 DCA between proton and pion

For DCA between proton and pion, we change the up-limit to be 0.15 smaller than original value, the QA figures are shown below. Again, Bin-0 is combination of all three bins, Bin-1 is $\ell/\beta\gamma$ [2,8], Bin-2 is $\ell/\beta\gamma$ [8,13] and Bin-3 is $\ell/\beta\gamma$ [13,25]. Figure 48 shows the signal numbers and Figure 7 shows the invariant mass plots. The uncertainty from DCA23 is 2.58%.

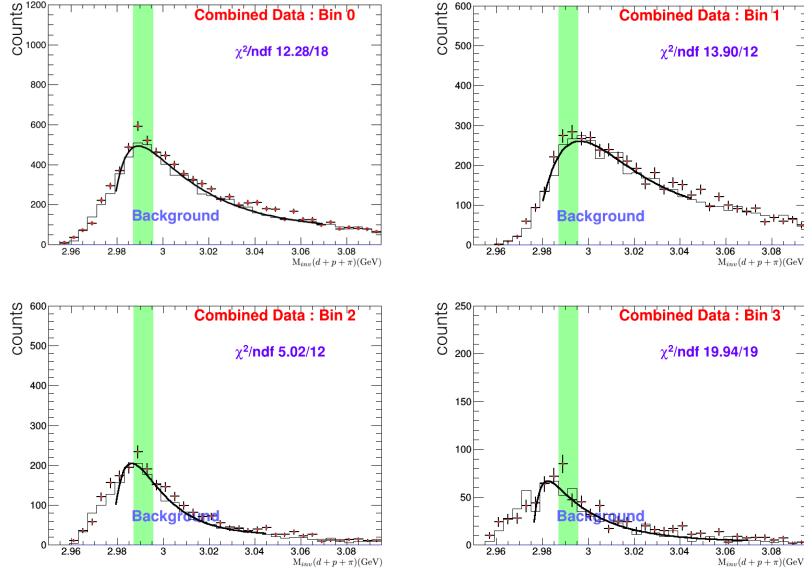


Figure 48: Invariant mass of ${}^3_{\Lambda}\text{H}$ in systematic uncertainty analysis from source : DCA between proton and pion. Bin-0 is combination of all three bins. Bin-1 is $\ell/\beta\gamma$ [2,8], Bin-2 is $\ell/\beta\gamma$ [8,13] and Bin-3 is $\ell/\beta\gamma$ [13,25].

7.1.3 DCA Between (virtual) Lambda and Primary Vertex

For DCA between lambda and PV, we change the up-limit to be 0.2 smaller than original value. And the QA figures (Figure 8) are shown below. Figure 49 shows the signal counts and efficiency. The uncertainty from DCA-lambda is 14.95%.

7.1.4 Other sources

Some embedding configurations may also cause systematic uncertainty. We consider the p_T distribution and $c\tau$ distribution as main sources. For p_T , we re-weight it with function 10. While parameter $p_0 = 1$ and $p_1 = 0.450$. For $c\tau$, we re-weight it to 145ps.

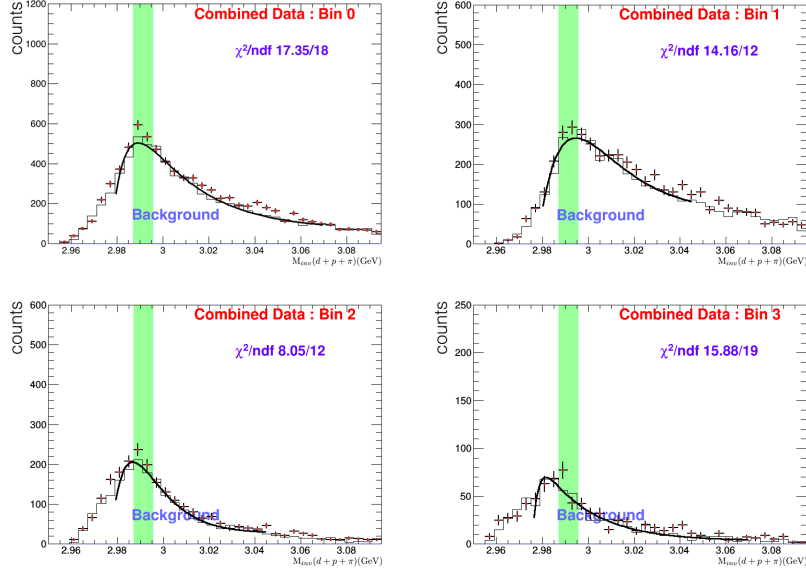


Figure 49: Invariant mass of ${}^3_{\Lambda}\text{H}$ in systematic uncertainty analysis from source : DCA between p- π pair to PV. Bin-0 is combination of all three bins. Bin-1 is $\ell/\beta\gamma$ [2,8], Bin-2 is $\ell/\beta\gamma$ [8,13] and Bin-3 is $\ell/\beta\gamma$ [13,25].

$$p_T(\text{weighted}) = p_0 \times x \times e^{-\frac{\sqrt{x^2 + 2.991^2} - 2.991}{p_1}} \quad (10)$$

The result shows, for 2-body analysis, the systematic uncertainty from embedding data are 6.50% and 4.93% for 2-body and 3-body analyses, respectively.

Additional sources of systematics, like loss of ${}^3_{\Lambda}\text{H}$ due to interactions between ${}^3_{\Lambda}\text{H}$ and the detector material or the air are also considered.

7.2 Two Body Part

7.2.1 Topological cuts and binning

We take into account two kinds of contributions to systematic errors: binning effect and different cuts.

- (1) Present result uses 4 MeV bin width and the fitted lifetime is 123 ± 26 ps. If bin width is changed to 2 MeV, the fitted lifetime is 116 ± 24 ps, thus the systematic error due to bin width is 5.7%.
- (2) Present V0 cuts: $\ell > 2.4$ cm, $\text{DCA}(\pi) > 0.8$ cm, $\text{DCA}_{1\text{to}2} < 1.0$ cm, $\text{DCA}_{v0} < 1.0$ cm.

- * New cuts set 1: $\ell > 4.0$ cm and $\text{DCA}(\pi) > 1.2$ cm. Result: 120 ± 30 ps.
- * New cuts set 2: $\text{DCA1to2} < 0.7$ cm and $\text{DCA}v0 < 0.7$ cm. Result: 130 ± 28 ps.

Thus systematic error due to cuts selection is 6.2%.

7.2.2 Interaction with Material

We consider the possible absorption effect from the interaction between hypertriton and material (air and detector structure material).

7.2.3 interaction with air

The absorption can be estimated by this formula:

$$e^{-\frac{\sigma(\Lambda^3 \text{H+air})}{\sigma(p+\text{air})} \cdot \frac{l}{\lambda_T/\rho}} \sim e^{-\frac{\sigma(\Lambda^3 \text{H+air})}{\sigma(p+p)} \cdot \frac{l}{\lambda_T/\rho}} \leq e^{-\frac{\sigma_{pd} + \sigma_{p\Lambda}}{\sigma_{pp}} \cdot \frac{l}{\lambda_T/\rho}} \quad (11)$$

From PDG database, $\sigma_{pp}=41$ mb, $\sigma_{pd}=83$ mb, $\sigma_{p\Lambda}=35$ mb (a reasonable p_{lab} range is selected). $\lambda_T=61.3$ cm, $\rho = 1.205 \times 10^3 \text{ g/cm}^3$. Therefore,

$$e^{-\frac{\sigma_{pd} + \sigma_{p\Lambda}}{\sigma_{pp}} \cdot \frac{l}{\lambda_T/\rho}} = e^{-\frac{l}{17.7 \times 10^3 (\text{cm})}} \quad (12)$$

Since decay length is to the magnitude of several centimeters, this absorption due to the interaction between hypertriton and air can be neglected.

7.2.4 Interaction with detector structure material

Using the same method as above, we can estimate the absorption by structure material is less than 1.5%, which can also be neglected.

7.3 Summary

The detailed numbers of systematic uncertainty study for lifetime and ratio are listed below in table 3 and table 4.

The combined uncertainty for lifetime calculation is 21.66%, and total systematic uncertainty for ratio is 25.06%. So, finally, with systematic uncertainty, the combined lifetime is:

$$c\tau = 142_{-21}^{+24} (\text{stat.}) \pm 31 (\text{syst.})$$

ratios is:

$$\text{Ratio} = 0.32 \pm 0.05 (\text{stat.}) \pm 0.08 (\text{syst.})$$

Table 3: Systematic uncertainty summary for lifetime measurement.

source	from 2-body (%)	source	from 3-body (%)
Binning	5.69	Binning	8.76
decay length and $\text{dec}\pi^-$	2.44	dca23	2.58
dca12 and dca0	5.69	dca Λ	14.95
p_T and $c\tau$	6.50	p_T and $c\tau$	4.93
background shape	3.54	background shape	3.54
Total	11.20		18.54

Table 4: Systematic uncertainty summary for ratio measurement

source	ratio uncertainty (%)
Binning	1.38
dca23	0.70
dca Λ	0.60
p_T and $c\tau$	25.00
Total	25.06

8 World Lifetime and Discussion

We also put a summary plot of the worldwide ${}^3_\Lambda\text{H}$ lifetime measurements as shown in figure 50. There have been discussions of the lifetime of ${}^3_\Lambda\text{H}$ since the 1960s. For many years, the ${}^3_\Lambda\text{H}$ was considered as a weakly-bound state formed of a deuteron and a Λ , which leads to the inference that the ${}^3_\Lambda\text{H}$ lifetime should be very close to that of the free Λ . However, not all experimental measurements support this picture. From the results in Figure 50, it can be seen that there are at least two measurements [15, 18] prior to the relatively recent heavy-ion work which indicate that ${}^3_\Lambda\text{H}$ has a shorter lifetime than the Λ . The lifetime measurement in [18] has the smallest error among similar studies in the 1960s and 70s, and was shorter than the others. This measurement was based on the 3-body decay channel ${}^3_\Lambda\text{H} \rightarrow p + d + \pi^-$ in a nuclear emulsion experiment. The shorter lifetime was attributed to the dissociation of the lightly-bound Λ and deuteron when traveling in a dense medium. However, this explanation is not very satisfying, since [16, 17, 20] also used nuclear emulsion, yet their measurements were close to the Λ lifetime. In addition, Ref. [15] used a helium bubble chamber and should not be affected by the hypothesized dissociation, yet their lifetime was also lower than free Λ . The likelihood method used to extract the lifetime from the detected samples becomes unreliable when the sample statistics are low.

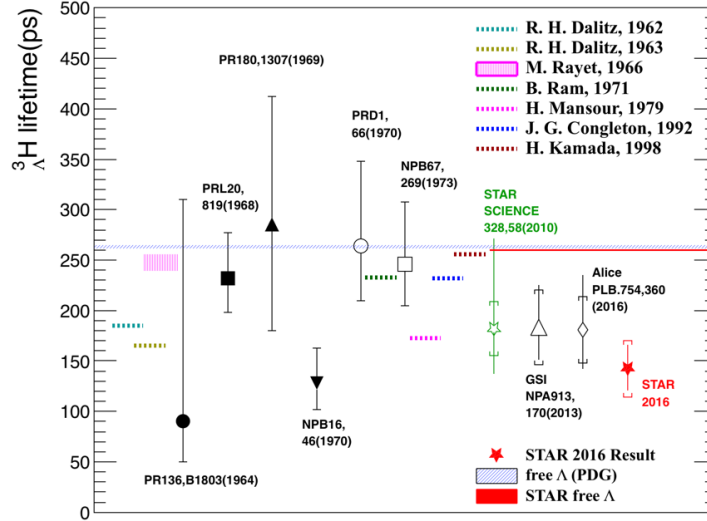


Figure 50: The world data comparison for lifetime of ${}^3_\Lambda\text{H}$ in history. Including theoretical calculation and experimental measurements.

A recent statistical compilation of the lifetime measurements available in the literature favors the lifetime of ${}^3_{\Lambda}\text{H}$ being shorter than that of the Λ [34, 35]. The present lifetime measurement casts further doubt on the early inferences concerning the structure of the ${}^3_{\Lambda}\text{H}$. The lifetime is related to the binding energy of Λ in hypernuclei and its decay channels. Theoretical predictions need to employ assumptions about the Λ binding energy, which is poorly measured [11, 12]. Assuming a larger binding energy leads to a shorter lifetime [10]. The current measurements clearly motivate further theoretical study [36].

In July 14th, 2017, ALICE Collaboration presents its new lifetime measurement in SQM, which yields a high value of hyper triton lifetime, see figure 51. We carry out a cross-check to see whether the new data is consistent with our measurement or not. Because the data points are not released yet, we take it by hand (not very accurate) from the figure 51. We do a χ^2 analysis with STAR data (7 data points) and ALICE preliminary result (4 data points), and find that the χ^2/NDF is reasonable, shown in figure 52.

In figure 53 we also show our ratio result with two early measurements. In the plot, the x-axis is the $\frac{p^2}{p^2+s^2}$, where p and s is the amplitudes for the $l_{\pi} = 0$ and $l_{\pi} = 1$ channel, the y-axis is R_3 . The two black curves are theoretical calculation of R_3 with 1/2 and 3/2 spin, respectively. The black result are from Bertrand's result in 1970, the blue point is the result of Keyes in 1973, which is a average summarization of several early measurement. The red star is our result. This plot indicates that our result is close to Keyes, and is between the 1/2 and 3/2 spin but slightly favors the 1/2 spin.

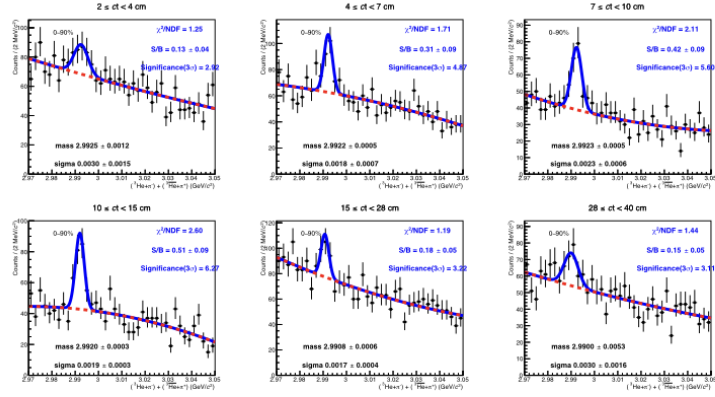


Fig. 6: $({}^3\text{H} + {}^3\text{H})$ invariant mass spectra for 6 ct bins, with superimposed the fit function (blue curve), used to extract the raw yields, and the background (red dashed curve).

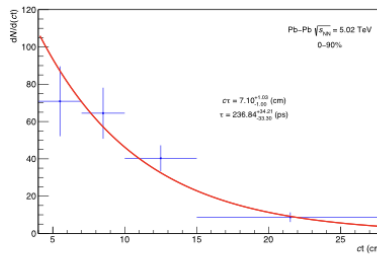


Fig. 9: Corrected yields vs ct (only stat. uncertainty). Points are fitted with an exponential function using the integral of the function in the full bin instead of the value at bin center.

Figure 51: The ALICE new preliminary results on hypertriton lifetime measurements.

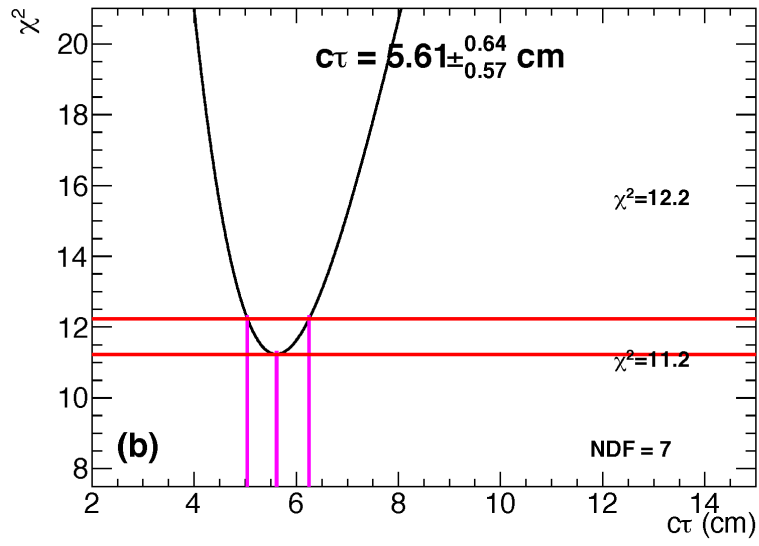


Figure 52: The χ^2 distribution from a combined analysis with STAR data and ALICE preliminary result.

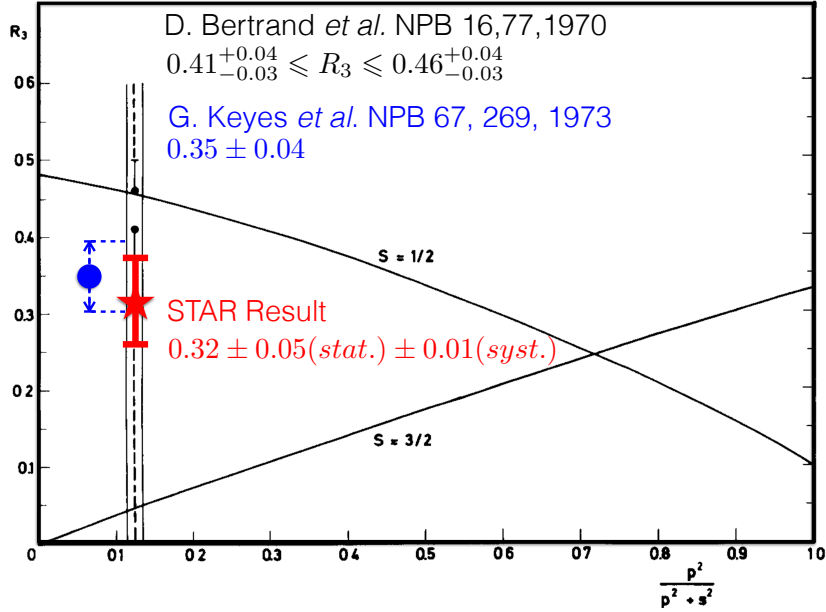


Figure 53: The comparison of our ratio result with early results. The x-axis is the $\frac{p^2}{p^2 + s^2}$, the y-axis is R_3 . The two black curves are theoretical calculation of R_3 with 1/2 and 3/2 spin, respectively. The black result are from Bertrand's result in 1970, the blue point is the result of Keyes in 1973, which is a average summarization of several early measurement. The red star is our result.

References

- [1] Elena Botta, Tullio Bressani, and Gianni Garbarino. Strangeness nuclear physics: a critical review on selected topics. *Eur. Phys. J. A*, 48:41, 2012.
- [2] H. Müller and J. R. Shepard. $\Lambda - \Sigma^0$ mixing in finite nuclei. *J. Phys. G.*, 26:1049, 2000.
- [3] J. M. Lattimer and M. Prakash. The physics of neutron stars. *Science*, 304:536, 2004.
- [4] Jürgen Schaffner-Bielich. Hypernuclear physics for neutron stars. *Nucl. Phys. A*, 804:309, 2008.
- [5] P. B. Demorest et al. A two-solar-mass neutron star measured using shapiro delay. *Nature*, 467:1081, 2010.
- [6] John Antoniadis et al. A massive pulsar in a compact relativistic binary. *Science*, 340:448, 2013.

- [7] S. Weissenborn, D. Chatterjee, and J. Schaffner-Bielich. Hyperons and massive neutron stars: Vector repulsion and SU(3) symmetry. *Phys. Rev. C*, 85:065802, 2012.
- [8] Luiz L. Lopes and Debora P. Menezes. Hypernuclear matter in a complete SU(3) symmetry group. *Phys. Rev. C*, 89:025805, 2014.
- [9] R. O. Gomes, V. Dexheimer, S. Schramm, and C. A. Z. Vasconcellos. Many-body forces in the equation of state of hyperonic matter. *The Astrophys. J.*, 808:8, 2015.
- [10] R. H. Dalitz and G. Rajasekharan. The spins and lifetimes of the light hyper nuclei. *Phys. Lett.*, 1:58, 1962.
- [11] H. Kamada et al. π -mesonic decay of the hypertriton. *Phys. Rev. C*, 57:1595, 1998.
- [12] M. Juric et al. A new determination of the binding-energy values of the light hypernuclei ($A \leq 15$). *Nucl. Phys. B*, 52:1, 1973.
- [13] M. Rayet and R. H. Dalitz. The lifetime of ${}^3_{\Lambda}\text{H}$. *Nuovo CIMENTO*, 46:786, 1966.
- [14] M. M. Block et al. Hyperfragment study in the helium bubble chamber. *Proc. of the Inter. Conf. on Hyperfragments, CERN Report*, 64-1:63, 1964.
- [15] R. J. Prem and P. H. Steinberg. Lifetime of hypernuclei, ${}^3_{\Lambda}\text{H}$, ${}^4_{\Lambda}\text{H}$, ${}^5_{\Lambda}\text{H}$. *Phys. Rev.*, 136:B1803, 1964.
- [16] G. Keyes et al. New measurements of the ${}^3_{\Lambda}\text{H}$ lifetime. *Phys. Rev. Lett.*, 20:819, 1968.
- [17] R. E. Phillips and J. Schneps. Lifetime of light hyperfragments. *Phys. Rev.*, 180:1307, 1969.
- [18] G. Coremans et al. On the lifetime of the ${}^3_{\Lambda}\text{H}$ hypernucleus. *Nucl. Phys. B*, 16:46, 1970.
- [19] G. Keyes et al. Properties of ${}^3_{\Lambda}\text{H}$. *Phys. Rev. D*, 1:66, 1970.
- [20] G. Keyes, J. Sacton, J. H. Wickens, and M. M. Block. A measurement of the lifetime of the ${}^3_{\Lambda}\text{H}$ hypernucleus. *Nucl. Phys. B*, 67:269, 1973.
- [21] B. I. Abelev et al. Observation of an antimatter hypernucleus. *Science*, 328:58, 2010.

- [22] C. Rappold, E. Kim, D. Nakajima, T. R. Saito, and O. Bertini. Hypernuclear spectroscopy of products from ${}^6\text{Li}$ projectiles on a carbon target at 2 A GeV. *Nucl. Phys. A*, 913:170, 2013.
- [23] J. Adams et al. ${}^3_\Lambda\text{H}$ and ${}^4_\Lambda\text{H}$ production in Pb-Pb collisions at $\sqrt{s_{\text{NN}}}=2.76\text{TeV}$. *Phys. Lett. B*, 754:360, 2016.
- [24] R. H. Dalitz and L. Liu. Pionic decay modes of light Λ hypernuclei. *Phys. Rev.*, 116:1312, 1959.
- [25] M. M. Block and R. H. Dalitz. Structure of the interaction $\lambda+n \rightarrow n+n$. *Phys. Rev. Lett.*, 11:96, 1963.
- [26] B. Ram and W. Williams. Decay rate and branching ratio ($\pi^- + {}^3\text{He}$)/(all π^- modes) of ${}^3_\Lambda\text{H}$. *Nucl. Phys. B*, 28:566, 1971.
- [27] H. M. M. Mansour and K. Higgins. The decay rate of ${}^3_\Lambda\text{H}$. *Nuovo CIMENTO*, 51:180, 1979.
- [28] N. N. Kolesnikov and V. A. Kopylov. Meson decays of hypertritium. *Sov. Phys. J.*, 31:210, 1988.
- [29] J. G. Conleton. A simple model of the hyper triton. *J. Phys. G*, 18:339, 1992.
- [30] K. H. Ackermann et al. STAR detector overview. *Nucl. Instrum. Methods A*, 499:624, 2003.
- [31] M. Anderson et al. The STAR time projection chamber: a unique tool for studying high multiplicity events at RHIC. *Nucl. Instrum. Methods A*, 499:659, 2003.
- [32] R. G. Ammar, W. Dunn, and M. Holland. On the spin and binding of ${}^3_\Lambda\text{H}$. *Nuovo CIMENTO*, 26:840, 1962.
- [33] D. Bertrand et al. Branching ratios for the π^- mesonic decays of the hypernuclei ${}^3_\Lambda\text{H}$ and ${}^4_\Lambda\text{H}$. *Nucl. Phys. B*, 16:77, 1970.
- [34] K. A. Olive et al. Particle Data Group. *Chin. Phys. C*, 38:090001, 2014.
- [35] C. Rappold et al. On the measured lifetime of light hypernuclei ${}^3_\Lambda\text{H}$ and ${}^4_\Lambda\text{H}$. *Phys. Lett. B*, 728:543, 2014.
- [36] A. Gal, E. V. Hungerford, and D. J. Millener. Strangeness in nuclear physics. *Rev. of Mod. Phys.*, 88:035004, 2016.